International Journal of Fatigue 132 (2020) 105358

Contents lists available at ScienceDirect

International Journal of Fatigue

journal homepage: www.elsevier.com/locate/ijfatigue

Fatigue of additive manufactured Ti-6Al-4V, Part I: The effects of powder feedstock, manufacturing, and post-process conditions on the resulting microstructure and defects

J.W. Pegues[a,b], S. Shao[a,b,*], N. Shamsaei[a,b], N. Sanaei[c], A. Fatemi[d], D.H. Warner[e], P. Li[e], N. Phan[f]

[a] Department of Mechanical Engineering, Auburn University, Auburn, AL 36849, USA
[b] National Center for Additive Manufacturing Excellence (NCAME), Auburn University, Auburn, AL 36849, USA
[c] Department of Mechanical, Industrial and Manufacturing Engineering, University of Toledo, Toledo, OH 43606, USA
[d] Department of Mechanical Engineering, University of Memphis, Memphis, TN 38152, USA
[e] Cornell Fracture Group, School of Civil and Environmental Engineering, Cornell University, Ithaca, NY 14853, USA
[f] Structures Division, U.S. Naval Air Systems Command (NAVAIR), Patuxent River, MD 20670, USA

ARTICLE INFO

Keywords:
Additive manufacturing
Microstructure
Post-processing
Defects
Process parameters

ABSTRACT

Additive manufacturing provides an appealing means to process titanium alloy parts with new levels of conformability, complexity, and weight reduction. However, due to the heating/cooling rates and heat transfer associated with directed energy source material processing, the as-built AM parts contain unique material and microstructural features. In order to confidently manufacture fatigue critical additive manufactured (AM) Ti-6Al-4V parts, a better understanding of the interrelationships between powder feedstock, AM processes, structure of the processed parts, their resulting mechanical properties, and their performance under realistic loadings is necessary. Part I of this two-part collection focuses on the powder-process-structure relationships and how powder feedstock, manufacturing, and post-processing conditions can affect the microstructure and defect features that ultimately contribute to the fatigue performance of Ti-6Al-4V parts. The material and physical phenomena inherent to the AM process of Ti-6Al-4V are discussed in detail and related to the phase composition/structure, grain morphology, surface characteristics, defect size/distribution, and post-process treatments available for AM parts. This investigation is the foundation for the structure-performance relationships that will be discussed in detail in Part II.

1. Introduction

Additive manufacturing (AM), as opposed to traditional reductive manufacturing such as milling, turning and drilling, can build near-net-shaped parts from the "bottom-up" in a layer-by-layer fashion as guided by a computer-aided drawing (CAD) model [1,2]. Machining and assembly steps can be eliminated through the use of AM, which can significantly reduce the fabrication and assembly time for complex Ti-6Al-4V parts [3–5]. AM can also be used to deposit new material atop damaged/worn components per user-designed profiles, enabling the repair of components that are otherwise too expensive or not feasible to replace [3–5]. The layer-wise nature of AM enables the production of parts with relatively complicated geometries, such as lattice-like metastructures [4] that were previously exceedingly expensive, if not impossible, to make.

AM technology is referred to using several different designations [3,6,7]. Depending on the specific apparatus used, these technologies may be categorized according to the energy source including laser, electron beam, and plasma; and material feedstock form including powder bed, blown powder, and wire feeding [6]. Despite these differences, AM technologies (excluding sintering) share the same basic methodology - a mobile melt pool is formed by a directed energy

Abbreviation: AM, additive manufacturing/additive manufactured; BCC, body centered cubic; CAD, computer aided design; CIS, crack initiation site; EBM, electron-beam melting; EVS, extreme value statistics; FCC, face centered cubic; FCO, face centered orthorhombic; GPD, generalized Pareto distribution; HCF, high cycle fatigue; HCP, hexagonal closed packed; HT, heat treatment; HIP, hot isostatic pressing; HV, vickers hardness number; LOF, lack-of-fusion; ME, mean excess; PSP, process-structure-property; SRμT, synchrotron radiation micro-tomography; UTS, ultimate tensile strength; VHCF, very high cycle fatigue; YS, yield strength; LB-PBF, laser beam powder bed fusion

* Corresponding author at: Department of Mechanical Engineering, Auburn University, Auburn, AL 36849, USA.
E-mail address: sshao@auburn.edu (S. Shao).

https://doi.org/10.1016/j.ijfatigue.2019.105358
Received 30 August 2019; Received in revised form 25 October 2019; Accepted 29 October 2019
Available online 02 November 2019

Nomenclature

α	alpha phase
α', α''	martensite phases
α'_m	massive phase
β	beta phase
ρ	part density
ρ_{wrt}	part density of wrought
Ω_α	atomic volume of alpha phase
Ω_β	atomic volume of beta phase
a_α	lattice constant of alpha phase
a_β	lattice constants of beta phase
area	defect area normal to the applied stress
c_α	lattice constant of alpha phase
E	power density
E_{opt}	optimum power density
f	volumetric stock feed rate
g	energy absorption coefficient
G	thermal gradient
h	hatch spacing
P	power of the heat source
t	deposited thickness
V	scan speed
Q	solidification rate

source, which performs line scans according to a predetermined CAD scan strategy. These line scans are repeated to consolidate a layer of solid material, and the part is then built incrementally layer-by-layer in a "bottom-up" fashion. The setup and operations of AM machines is covered in great detail by numerous reviews [8–11] and will not be reiterated in this work.

Titanium alloys such as Ti-6Al-4V are used extensively in the biomedical and aerospace industries due to their high strength, low density, biocompatibility, excellent corrosion resistance, and acceptable high temperature properties. They are a proven workhorse in a broad range of engineering applications, such as air frames, jet engines, biomedical devices, and chemical processing equipment [10]. Given the general good weldability of titanium alloys, they quickly became popular for AM processes.

The mechanical behavior of Ti-6Al-4V, like other alloys, is governed by its underlying microstructural characteristics. Pure titanium is allotropic, having a BCC crystal structure (β phase) at high temperature and an HCP crystal structure (α phase) when cooled below 882 °C. The α-β transformation temperature (β-transus) is sensitive to chemical composition, and thus, alloying elements can be used to stabilize the α and/or β phase in a desired temperature range [10]. Commercial titanium alloys are categorized into three families based on their phase composition at service temperature: (1) α alloys and commercially pure titanium, (2) β alloys, and (3) α + β dual phase alloys. The most widely used titanium alloy is Ti-6Al-4V, which is a α + β dual phase alloy.

During production from a melt, Ti-6Al-4V solidifies as β phase then transitions to its α + β dual phase structure as it cools. If cooling rates are high enough, a martensitic transformation can occur, which produces an α′ phase that is metastable at room temperature. This phase is common in laser processed additive manufactured (AM) Ti-6Al-4V. Both the α and α′ phases nucleate and grow from phase boundaries, i.e. β – β, α – β, and α′- β depending on the cooling rate. The morphology of the α and α′ phases reflects the prior β microstructure that existed at high temperature. The evidence of the prior high temperature β structure in the room temperature microstructure is termed prior- β microstructure.

The unique characteristics of the AM heat source, i.e. its rapid movement, high intensity, and small size, bring challenges not encountered in traditional manufacturing. The prior β microstructure of AM Ti-6Al-4V parts can be highly textured, with aligned elongated grains [8,12–14]. This can lead to a textured final α′ – α - β microstructure [12] and contributes to the anisotropic mechanical/fatigue properties [10,15]. Optimal AM build parameters generally favor the formation of elongated prior-β grains along, or at a certain angle to, the build direction [12,14,16]. The formation of these elongated prior-β grains, combined with AM-driven epitaxial crystal growth, leads to the highly textured prior β microstructure [3].

AM Ti-6Al-4V parts typically contain microscopic defects, such as gas entrapment and flat lack-of-fusion (LOF) defects [3,4,17–22]. Such defects can degrade fracture toughness and ductility under monotonic

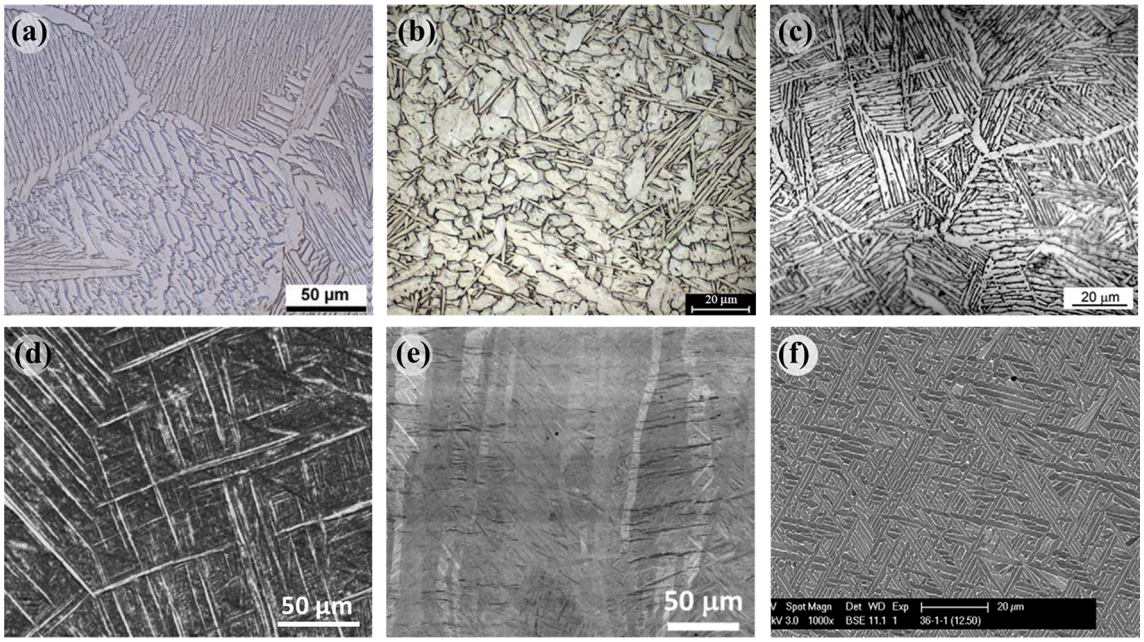

Fig. 1. Variety of Ti-6Al-4V microstructures resulting from AM and/or subsequent HT with (a) showing fully lamellar, (b) bimodal/duplex, (c) coarse Widmanstätten/basket weave, (d–e) acicular martensite, (f) fine Widmanstätten/basket weave. Reproduced with permission from Refs. [25,32,48,49,53,144].

loading [12,18,19,21–33]. Under cyclic loading, pores and LOF defects can overshadow any effects of microstructure, substantially degrading the fatigue life by serving as crack initiation sites (CIS) [22,34–36]. The LOF defects tend to be aligned perpendicular to the build direction. The presence of these LOF defects can result in strong anisotropy in the fatigue strengths of AM samples [22]. Optimization of AM process parameters has been shown to be successful in reducing the defect size and population by reducing LOF defects [37]. However, porosity, partially due to gas entrapment, still exists and reduces the fatigue strength of many AM materials. The presence of these gas entrapment pores in AM Ti-6Al-4V has significantly limited its use in fatigue critical applications and has driven recent research efforts to better understand the link between defects and mechanical behavior. Currently, much of the focus has been directed toward understanding the relationship between defect size and location on the resulting fatigue behavior [38]. To improve the mechanical properties and deal with the inherent defects, post-process treatments such as hot isostatic pressing (HIP) and traditional heat treatments or a combination of the two have proven necessary [39–43]. These post-process treatments affect both the defect size and distribution as well as the final microstructure.

The characteristics of the defect populations and microstructure in AM Ti-6Al-4V are controlled by many factors, e.g. component size and geometry, build system/parameters, batch size, powder feedstock, and more. This, together with the sensitivity of defect and microstructure characteristics on these factors, makes prediction complex [8,13,44] and can lead to substantial variability between AM machines, and even builds on the same machine in some cases [45]. This motivates the quest to better understand microstructure and defect formation/evolution during AM part processing, as well as the inter-relationship between build process, microstructural characteristics, and part performance (process-structure-property).

This two-part review on the fatigue behavior of AM Ti-6Al-4V aims to better illuminate the powder-process-structure-property-performance (PPSPP) relationships that are critical to producing fatigue critical parts. Part I reviews the physical aspects of the microstructure and defect evolution during the additive process, including post-processing, and centers on the process-structure portion of the overall PPSPP relation. This work lays the foundation for Part II, the review on the structure-property-performance relationships, with an emphasis on fatigue. While the review touches on aspects of many AM processes, a focus is given to powder bed fusion systems as they are the most prevalent in the literature and widely accepted across several industries [46].

2. Microstructure

2.1. Processing condition and phase compositions

Typical AM Ti-6Al-4V microstructures are shown in Fig. 1. It can be seen that with post-processing heat treatment (HT) and/or HIP, microstructures similar to conventional wrought Ti-6Al-4V can be produced - such as the fully lamellar structure shown in Fig. 1a and duplex/bi-modal structure shown in Fig. 1b. However, as discussed in later sections, HT schedules for AM parts often differ from the well-established wrought procedures. Without post-process treatments, the microstructure of as-built Ti-6Al-4V fabricated from electron beam powder bed fusion (EB-PBF) typically consists of a very fine Widmanstätten/basket weave structure (Fig. 1c) due to the high cooling rates ($10^3 \sim 10^5$ K/s [47]) combined with beam heated substrates (~970 K, higher than the decomposition temperature of martensitic phases) [28,29 32]. Laser-based AM has even higher cooling rates ($10^4 \sim 10^6$ K/s [47]) and build plates that are typically not heated to the extent of EB-PBF processes, and therefore tends to produce martensitic structures [32,48], which contains ultra-fine acicular features (Fig. 1d and e show typical α′ martensite phase). An ultrafine Widmanstätten (Fig. 1f) can also result from laser-based AM processes, since the repeated reheating during the fusion of subsequent layers may bring the part temperature above the martensite decomposition temperature [49 32]. The microstructure of Ti-6Al-4V is determined by the specific thermal history that a region of AM material has experienced, namely the repeated melting-solidification-reheating-cooling during the AM build and post-build heat treatment procedures. Below, a description of the continuous cooling behavior and the resulting phases of Ti-6Al-4V is provided for a broad range of cooling rates (from 0.05 K/s and below to 410 K/s and above), covering the typical scenarios encountered during AM and post-build HT.

Above the β–transus temperature, Ti-6Al-4V is purely in a BCC β phase (Fig. 2a). The grain size of the β phase depends on the cooling rate from the liquidus to solidus temperatures. Nucleation-dominated solidification is favored under higher cooling rates and this results in smaller β grain sizes, while grain growth dominated solidification is favored under lower cooling rates, resulting in larger β grain sizes.

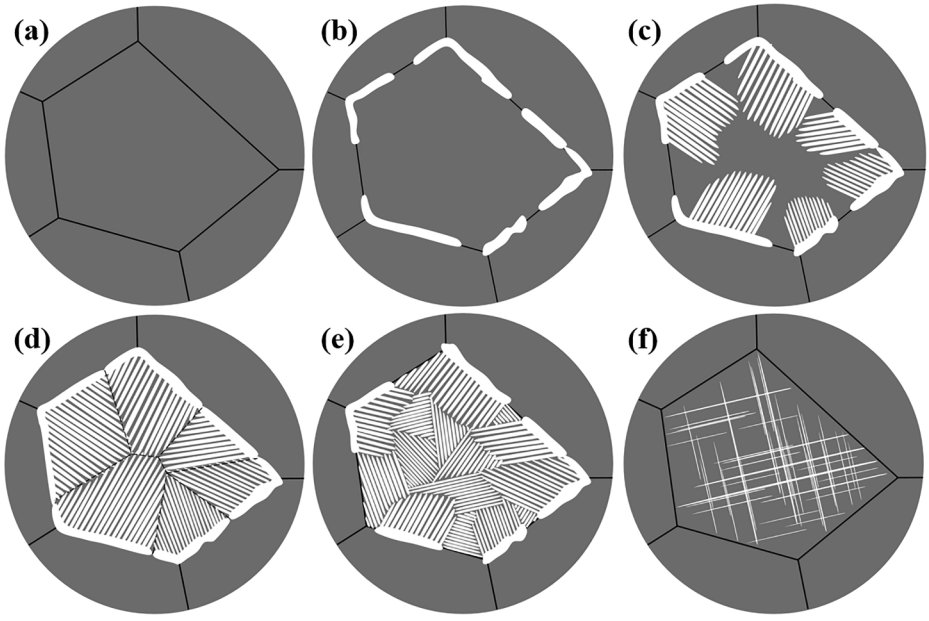

Fig. 2. Schematic illustrations of phase transformation mechanisms during continuous cooling of Ti-6Al-4V from temperatures above β–transus. Gray regions are β phase, white regions are α phase in (a)–(e), the grain in (f) with thin, orthogonal lines denotes a fully martensitic grain (can be α′ or α″), while the black lines are β grain boundaries. Note that only the phase transformation activity in the center grain is depicted in each subfig. for simplicity, although the surrounding grains experience the same phenomena.

When Ti-6Al-4V is cooled from above the β–transus temperature (1267 K), the resulting phase compositions and structures depend mostly on cooling rate (Fig. 2) [50,51] and prior β grain size, which is discussed in more detail below.

As the temperature drops below the β–transus temperature, the HCP α phase first nucleates and grows at/along grain boundaries and triple points of the β phase schematically illustrated in Fig. 2b. The length of the α phase that forms at the prior grain boundaries of the β phase depends on its nucleation vs growth rate and, to some extent, the size of the prior β grain. The interface between α and β phases is semi-coherent, i.e. it contains misfit dislocations. As cooling continues, the α phase nucleates and grows from the phase boundaries (Fig. 2c), as well as directly from the β grain boundaries (if it is not completely covered by grain boundary α). This α phase grows as a plate (lamella). In many cases, it occurs at a rate that perturbs the distribution of alloying elements such that neighboring plates are nucleated, leading to a lamellar structure of α and β phases. Such structures are often referred to as colonies.

If the cooling rate is relatively low, the α colonies grow and meet the ones emanating from the opposite side of the β grain, and a fully lamellar α + β microstructure is formed (Fig. 2d, Fig. 1a). In this case, the size of the colonies is governed by the prior β grain size. At increased cooling rates, the tendency for nucleating new colonies increases, and colonies will nucleate from existing ones. This leads to a reduction in the average colony size. The resulting microstructure is often referred to as Widmanstätten or basket weave (Fig. 2e), and is commonly observed in AM Ti-6Al-4V parts. Overall, higher cooling rates cause finer "weaving"; for example, the microstructure in Fig. 1f (wire-fed laser deposition, faster cooling) is much finer than Fig. 1d (electron beam melting, slower cooling) and contains inter-protruding α plates which indicate interrupted/poorly-developed α colonies due to rapid nucleation of α phase. During the β → α + β phase transformation, the α and β phase stabilizing elements, namely Al and V respectively, are redistributed into the respective phase. If Ti-6Al-4V is cooled at a sufficiently high rate, a total martensitic transformation is expected and pure α′ or α", or a combination of α′ and α" phases, are expected as shown in Fig. 2f. The martensitic transformation process occurs without diffusion; and therefore, the resulting phases have the same composition as the parent β phase. The α′ phase has an HCP crystal structure, but with slightly different lattice parameters than α, while the α" phase has a face centered orthorhombic (FCO) crystal structure [52].

A useful perspective of the Ti-6Al-4V phase composition is provided by the continuous cooling transformation (CCT) diagram. Fig. 3 shows CCT diagrams generated by two groups, i.e. Sieniawski et al. [51] and Ahmed and Rack [50]. According to Sieniawski et al. [51] (phase field boundaries coded in reddish colors in Fig. 3), when cooled from above the β–transus temperature (such as after homogenization at 1323.15 K used in a typical HT, and at reheating after solidification during AM) at cooling rates below 1.5 K/s, the β → α + β phase transformation starts at about 1250 K and finishes at 950 K.

At cooling rates higher than 10 K/s, the β → α″ martensitic transformation becomes active. However, when cooling rates are below 120 K/s, the α″ martensite is unstable and recovers to the α + β phase with continued cooling (phase field marked by dash dotted line in dark red). Microstructures such as fully lamellar and Widmanstätten can form for cooling rates below 120 K/s. At cooling rates higher than 120 K/s, β → α″ martensitic transformation (starts at 1125 K and finishes at 1000 K) takes over and the resulting phase is martensitic α″. It is worth mentioning that although the CCT diagram from Sieniawski et al. [51], suggests a pure β → α″ transformation, their accompanying works suggests both martensitic phases occur for Ti-6Al-4V i.e. β → α′(α″). This agrees with a number of other works [32,50].

Ahmed and Rack [50] suggest different phase transformation processes (phase boundaries and fields coded in bluish colors Fig. 3) for cooling rates above 20 K/s. At a cooling rate between 20 K/s and 410 K/s, the phase transformation is not purely martensitic β → α′(α″) or β → α″, as suggested by Sieniawski et al. [51]. Instead, the transformation is β → α + α′ + α'_m (light blue phase field in Fig. 3), where α'_m is a massive phase, with an HCP crystal structure identical to α′ phases. Cooling rates higher than 410 K/s, however, lead to β → α′ martensitic transformation below 848 K (in the cyan phase field in Fig. 3) and a pure α′ phase (such as shown in Figs. 1d, e and 2f) as a result. This cooling rate, and the associated martensitic microstructure are often observed in laser beam powder bed fusion (LB-PBF) processes.

The martensitic phases (α′, and α″) and the massive phase (α'_m) formed due to the fast cooling rates are meta-stable and decompose upon reheating [32]. The α′ phase decomposes upon reheating at temperatures as low as 673 K [32]. This suggests that a stress relieving HT, if performed above 673 K, decomposes the α′ martensite easily. The decomposition can also be achieved in situ during laser AM when previously deposited layers are repeatedly reheated and more slowly cooled due to the deposit of successive layers, as shown by Xu et al. [32]. Accordingly, an increased power density favors the decomposition of the α′ martensite during laser AM processes in that previously deposited layers will be more likely to experience slow cooling from above the martensite decomposition temperature. In EBM AM processes, the build chamber is evacuated and the powder bed can be held at an ambient temperature above the martensite decomposition temperature and slowly cooled at the finish of the build, leading to consistent α + β phase structure [28,29].

The crystallographic orientation relation between the HCP α and BCC β phases strictly follows the Burgers relationship of $[1\bar{1}1]_\beta // [11\bar{2}0]_\alpha$ and $(110)_\beta // (0002)_\alpha$, as shown in Fig. 4 [10]. The α plates are always parallel to the $(\bar{1}12)$ planes of the β matrix and the $(\bar{1}100)$ planes of the α phase. Since a BCC lattice has twelve independent {1 1 2} planes, there are twelve possible variants in the α-colony orientation inside a single prior β grain. In addition, lattice strain is associated with the β → α + β transformation. The lattice constant for the β phase is a_β = 3.32 Å, and a_α = 2.95 Å and c_α = 4.68 Å for the α phase. The atomic volumes for the two phases are Ω_β = 17.64 Å^3 and Ω_α = 18.30 Å^3, which corresponds to a volumetric strain of 3.6%. The β to α transformation stain is anisotropic with strains of 2.5% in the $[1\bar{1}1]_\beta$ direction, −0.3% in the $[110]_\beta$ direction, and 6% in the $[\bar{1}12]_\beta$ direction. To minimize the overall strain energy associated with the β → α + β phase transformation, the orientation of the α colonies tend to be "randomized". As a result, the population of α colonies in each orientation is roughly equal in a prior β grain.

The Widmanstätten structure, schematically shown in Figs. 2c, d and 3e, is perhaps the most commonly observed microstructure in EBM

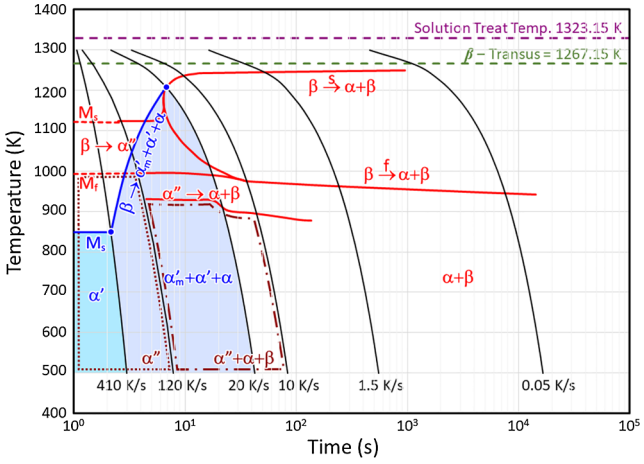

Fig. 3. Continuous cooling transformation (CCT) diagram for Ti-6Al-4V from above β–transus temperature to 500 K and showing the α″ (blue) and α′ (cyan) regions according to Refs. [50,51]. (For interpretation of the references to colour in this figure legend, the reader is referred to the web version of this article.)

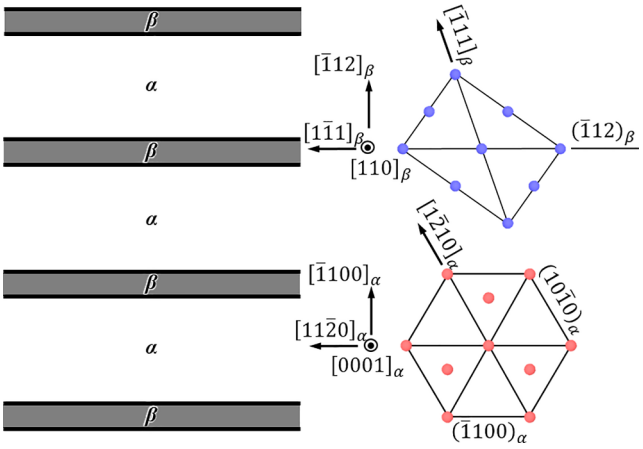

Fig. 4. Schematic illustration of the crystallographic orientation relation between α and β; image recreated based on Ref. [10]. The BCC β lattice is represented by blue atoms, while the HCP α lattice is represented by red atoms. (For interpretation of the references to colour in this figure legend, the reader is referred to the web version of this article.)

Ti-6Al-4V while the martensitic microstructure is mostly observed in LB-PBF Ti-6Al-4V. As previously discussed, the orientation of the α colonies/plates, although seemingly random, is well-defined and along any of the twelve {1 1 2} family planes in the prior β grain. The {1 1 2} planes always form certain angles with respect to each other, i.e. 33.6°, 48.2°, 60°, 70.5° and 80.4°. Fig. 5a shows three {1 1 2} planes, namely (112), $(\bar{1}12)$ and $(1\bar{1}2)$, as examples. Depending on the cutting plane, the trace of these three planes may form triangles with different angles. It is therefore very common to observe triangular patterns in very fine Widmanstätten microstructures. Fig. 5b–d show such patterns, marked by dashed lines, obtained from different studies. Note that the triangles have different angles due to the orientation of the α plates and the polishing planes.

This subsection has shown that the phase composition and structure of an AM Ti-6Al-4V part is dependent on its experienced thermal history, including initial cooling, and subsequent in-build reheating/cooling and annealing (such as one experienced with heated build plates). The phase structure ranges, in a decreasing order with cooling rate, from martensite (α′ and/or α″), fine Widmanstätten (α + β), coarse Widmanstätten, to fully lamellar (α + β). The martensite is metastable and is subject to decomposition due to the repeated reheating during AM process. For α + β microstructures, the thickness of individual α plates, as well as the size of the α colonies, decrease with increasing cooling rate. As will be discussed in Part II, these dimensions of the α colonies may affect the tensile and fatigue strengths of the Ti-6Al-4V parts, and are of critical relevance.

Many factors have been found to affect the cooling rate during AM. For instance, as was mentioned earlier, the EBM AM technologies have much higher ambient temperature compared to laser AM technologies, sometimes as high as $0.5T_m$, leading to much lower cooling rates, as evidenced by much coarser Widmanstätten structures [28,29,52,53]. It has been shown [32] that for LB-PBF, by varying the processing parameters, such as powder feed rate, scanning speed and laser power, cooling rates and the corresponding coarseness in phase structures can be controlled to some degree. In addition, the geometry of the build affects the cooling rate.

Even within the same build, the cooling rate may be very different depending on the local geometry. For instance, when the heat source is near the surfaces, the mass of material available to conduct heat away from the source can be much less than that in the bulk. It is well demonstrated [32] that if the location is thicker or connected to effective heat sinks, higher cooling rate is induced, vice versa. The last factor, among others, is the batch size, i.e. the number of parts being built simultaneously. Larger batch size means longer inter-layer time interval

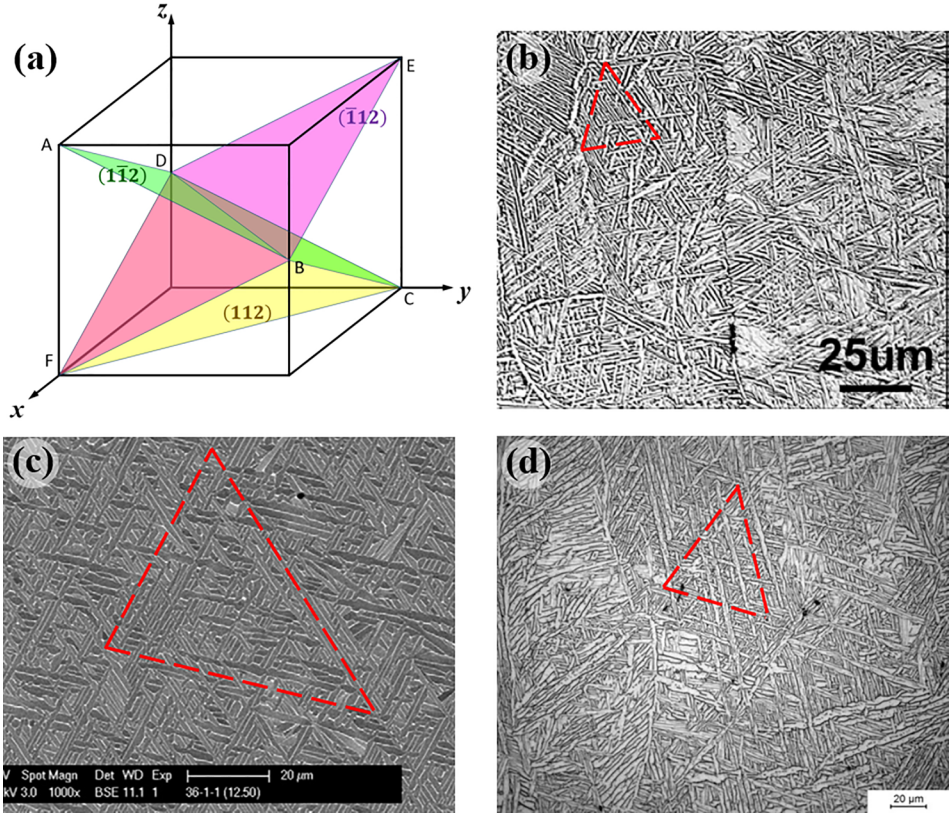

Fig. 5. Example {1 1 2} planes of a BCC lattice are shown in (a), while samples of very-fine Widmanstätten microstructures with α plates forming triangular patterns are shown in (b) [143], (c) [49] and (d) [49,142]. The microstructures shown are obtained from EBM (b & d) and shaped metal deposition (c).

(dwell time) for the part to cool down between each deposited layers, leading to much higher cooling rates and much finer α plates or martensitic transformation [44].

2.2. Prior β microstructure

Another important aspect of Ti-6Al-4V is its prior β microstructure before the solid-state phase transformations. Dictated by the process conditions in AM, the state of the prior- β microstructure before cooling below the β transus temperature can affect the final mechanical properties of AM Ti-6Al-4V [16]. The prior β microstructure remains evident after transformation to the HCP structure. The prior β grain size depends on the cooling rate experienced at and below the liquidus temperature (1893 K), while their morphology depends on both the thermal gradient and cooling rate [54,55]. Once Ti-6Al-4V is solidified, the prior β microstructure is usually stable and not easily altered through processes such as HT and HIP, unless the soak temperature reaches above the β-transus temperature [42,56]. As stated in Section 2.1, at lower cooling rates β microstructures affect the morphology of the α colonies, which in turn may affect the fatigue properties of Ti-6Al-4V. The prior β microstructure of AM Ti-6Al-4V shows strong [100] texture, which, together with the β grain size, can have a dominating impact on the fatigue properties of Ti-6Al-4V (as will be discussed in more detail in Section 5.2).

The β grains are not necessarily equiaxed, and thus the morphology of the β grains should be considered. β grain morphology is governed by both the thermal gradient and cooling rate [54,55] during solidification. In AM, typical solidification occurs via the growth of existing β crystals from the previously deposited layers as shown in Fig. 6. For typical melt pool sizes and shapes, crystal growth occurs in the trailing portion (right side of the dark green dashed line, blue shaded area) of the melt pool along the directions opposite to the direction of heat flux (red dashed arrows). In this case, a columnar β microstructure is formed that often shows a strong [100] texture in the growth direction. When the cooling rate is sufficiently high and the thermal gradients are sufficiently small, the β phase will nucleate away from the solid-liquid interface and equiaxed microstructures will form. Kobryn and Seiatin [57,58] used Hunt's model [59] to generate a solidification map for Ti-6Al-4V β microstructure morphology using the thermal gradient (G) and solidification rate (Q) as parameters (Fig. 7a). G is defined as the thermal gradient at the solidification boundary of the melt pool, and Q represents the cooling rate at the onset of solidification divided by the thermal gradient (G), i.e. $Q = 1/G(\partial T/\partial t)_{solidify}$.

As shown in Fig. 7a, the G-Q map is often partitioned into three regions, i.e. fully columnar, fully equiaxed, and mixed. Consistent with intuition, this map suggests that at low solidification rates and high thermal gradients, the β microstructure is fully columnar; and at low thermal gradients and high solidification rates, the microstructure is fully equiaxed. Considering that grain size is often controlled by the cooling rate (the product of G and Q), Fig. 7a provides a helpful illustration into how β grain size and morphology are related to the characteristics of the thermal field, with the solid black lines representing constant prior β grain size. For instance, when G and Q are adjusted along the black solid lines, β morphology changes from fully columnar to fully equiaxed, while the grain size is constant; within this same domain, when the cooling rate is changed (such as along the light red and blue arrows), grain size can be altered while maintaining the same grain morphology.

The parameters of the solidification map, G and Q, can be controlled through AM processing parameters, offering the opportunity to produce AM Ti-6Al-4V parts with tailored β microstructure. For example, Gockel et al. [8,13] have translated the solidification map to a processing map (Fig. 7b) for the wire-fed, electron beam deposition of a single bead. Their work shows that high absorbed power and scan velocity leads to fully equiaxed microstructure, while low absorbed power or scan velocity leads to fully columnar microstructure. The processing map utilizes parameters such as absorbed power and scanning velocity, which are directly tunable in several AM processes allowing limited microstructural control depending on the desired application.

The process map of the melt pool geometry (Fig. 7c) displays striking similarity to that of the microstructure. The lines of the constant cooling rate/grain size (black lines in Fig. 7b) are similar to those marking the constant melt area (solid lines with markers in Fig. 7c). The area of the melt pool is defined using the cross section perpendicular to scan direction at the maximum melt pool depth (dark green dashed line Fig. 6). The boundaries of the grain morphologies (blue solid and red dashed lines in Fig. 7b) are similar to the constant melt pool shape lines (L/d lines in Fig. 7c, dashed lines with marker); L/d is defined as the length of the melt pool along the scan direction divided by the maximum melt pool depth (Fig. 6). Fig. 7b and c suggest that closed-loop, on-the-fly control of the Ti-6Al-4V microstructure may be possible by monitoring the melt pool geometry during AM and providing real-time feedback to the processing parameters. This concept is developed further in Section 4 for in-situ monitoring and real time control of AM processes.

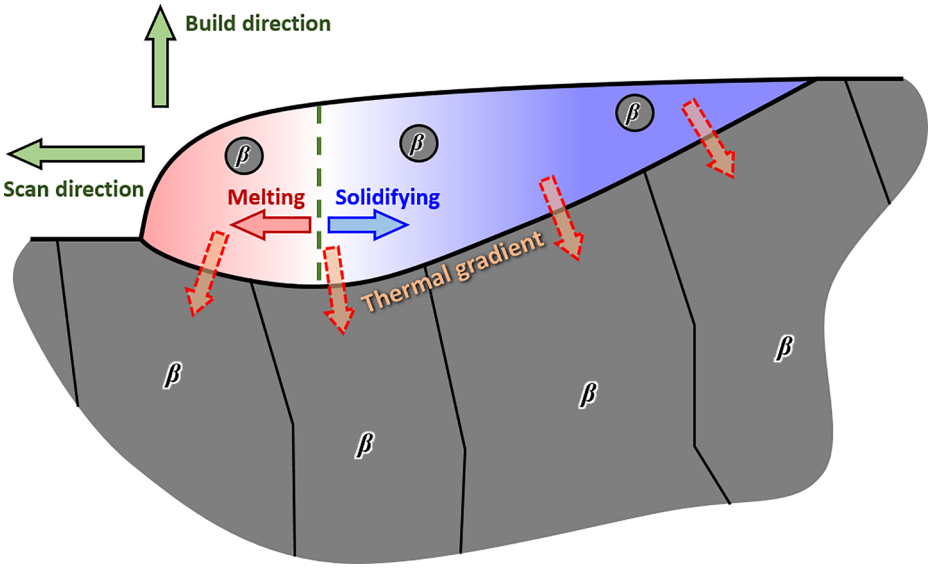

Fig. 6. Schematic illustration of the melt pool during AM.

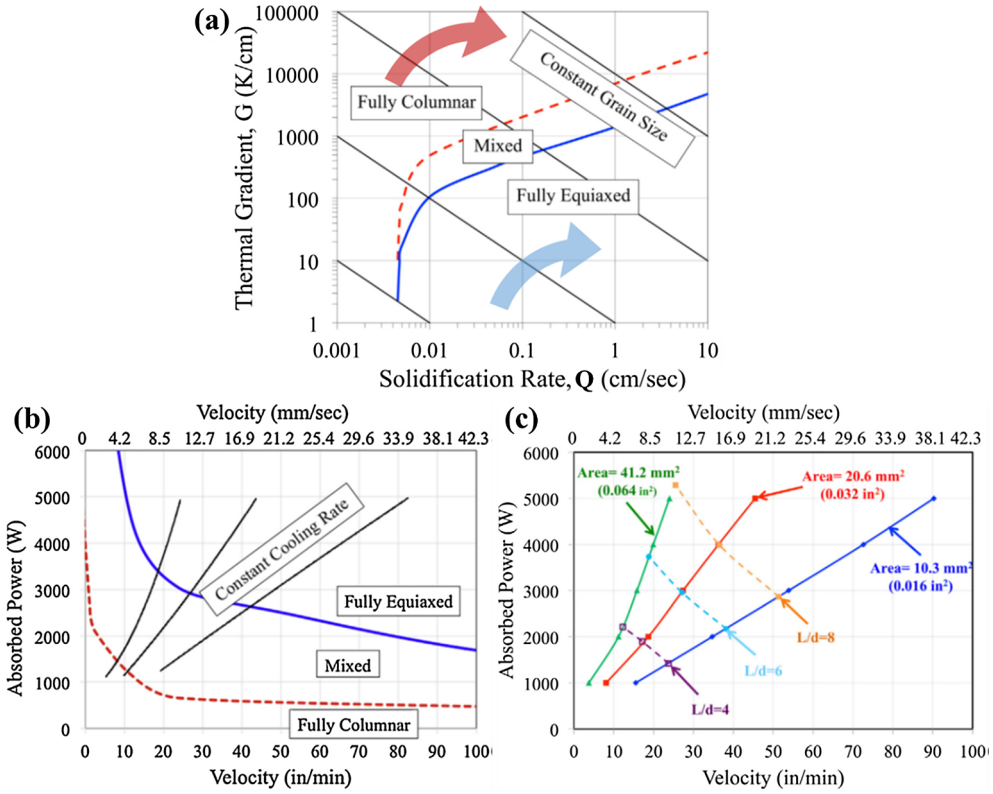

Fig. 7. (a) Solidification map for Ti-6Al-4V as a function of thermal gradient and solidification rate. (b) Process map for controlling prior β microstructure of Ti-6Al-4V of single bead deposits. (c) Process map for controlling melt pool dimensions for single bead deposits of Ti-6Al-4V. Images reproduced with permission from Ref. [8].

3. Defect formation, characterization, and statistical representation

3.1. Effect of process parameters on surface roughness

From the beginning, surface roughness has been a concern for the mechanical properties of AM parts, although surface roughness can be desirable in biomedical applications where biointegration is important. This is particularly true for fatigue performance, where microscopic features can act as CIS and substantially impact performance [60,61]. First, the layer-by-layer nature of the AM build process makes surface roughness unavoidable when geometries involve surfaces that are not parallel to the build plane or its normal direction. This has often been referred to as the stair casing effect [62]. Second, in powder bed approaches, the existence of partially melted particles attached to the surfaces leads to surface roughness. In both cases, the phenomena are outside the realm of traditional materials and specific to AM. Surface roughness is significantly influenced by process type, geometry and orientation, powder size, and process parameters such as laser power, scan rate, scan-line or hatch spacing, and layer thickness [63].

A linear model correlating laser power and surface roughness has been proposed for LB-PBF Ti-6Al-4V parts in [64]. At a constant speed of 250 mm/s and hatch spacing of 78 μm, increasing the laser power from 35 to 50 W led to a substantial drop of the arithmetic mean surface roughness, Ra, from 21 to 9 μm. This indicates that increasing the laser power could reduce the roughness for SLM parts for both top surfaces due to the flattening of melt pool and side surfaces due to elimination of balling phenomenon. They argued that higher laser power generates large vapor recoil pressures, which then cause the melt pool to flatten resulting in a better quality of the top surface. Moreover, when laser power increases, increased energy density results in improved wettability of the melt pool which eliminates surface tension variation between the previous solidified layer and the newly distributed powder layer. This reduces the chance of the balling phenomenon, and dramatically reduces the side surface roughness. On the other hand, conditions in the melt pool that induce balling of the molten material can disrupt the edge of the melt pool and affect the shape of the layer edge.

In contrast, another study analyzing the top and side surface roughness of laser beam melted parts showed that there is a compromise between them, i.e. improving the R_a on the top is always accompanied by deterioration R_a of the side and vice versa [65]. Different surface tensions as a result of temperature variations within the melt pool were mentioned as the reason which leads to a type of balling in which the melt pool breaks up into small enteties along the edge to alleviate these fluctuations in surface tensions. Also, larger size of and increased overlapping area between melt pools have been shown to improve the surface roughness significantly [66]. At a constant hatch spacing, with increasing scanning speed, the melt pool size reduces. A decrease in melt pool size reduces the overlap, which results in a higher roughness for the top surface. Moreover, while the melt pool is solidifying, the surrounding, partially melted powder particles stick to the edge of the layer, which contributes to the final surface roughness. This fact suggests that lower laser power can result in less time above the melting temperature and ultimately lower surface roughness on the sides of the part.

The layer-by-layer production process in AM results in a high dependence of the surface characteristics on the inclination angles, which are defined as the angles between the manufactured parts with respect to the build direction. As-built LB-PBF specimens fabricated in a diagonal direction with respect to the build plate show a distinct surface roughness. The roughness is higher for the downward-facing surfaces (down-skin) compared to the upward-facing surfaces (up-skin) [60,67]. For both up- and down-skin surfaces that are fabricated diagonally from the substrate, the staircase effect can increase the roughness. Down-skin surfaces pose an even bigger challenge as there is minimal part volume beneath the edge. Since these surfaces are practically built on the powder, whose thermal conductivity is approximately an order of magnitude lower than the solidified section, more powder particles are partially melted to the surface resulting in much higher surface roughness than the up-skin surfaces [60]. This dependence of surface roughness on location within the inclined specimen can be correlated to the experienced thermal history via a linear heat conduction model

[45]. The down-skin locations of two different geometries both had higher surface roughness compared to the up-skin surfaces, and accordingly, the thermal model predicted higher temperature histories on the down-skin surfaces [45], as shown in Fig. 8c.

Melt pool on unsupported layers is also affected by gravity which makes them sag into the un-melted powder underneath and creates much rougher down–skin surfaces than up-skin surfaces [68]. Down-–skin surfaces with angles less than 45° from the substrate typically associates with poor surface quality and are usually avoided by reorienting the part or by adding support structures. The reorientation is preferred to avoid the need for building of support structures, as their removal from the part can lead to additional defects such as burrs contributing to even higher roughness [69]. Orientation of the part during fabrication can therefore have significant effects on the surface roughness of AM parts and must be taken into consideration during the design stages prior to fabrication.

3.2. Characterization of the surface roughness

Roughness profiles caused by outmost adhered powder can be captured by standard stylus profilometry. Careful consideration is required for selection of the stylus cone angle and tip radius in order to provide surface measurements with minimal mechanical filtering of the data while also avoiding damage to the surface, particularly along steep features that could induce considerable lateral loads. It is also necessary to consider the accessibility of the features such as overhangs or reentry points which can be missed through contact profilometry. Stylus surface profilometers have been widely used to evaluate the surface quality of the AM parts and, based on a study published in 2016, the common measurement method used for AM was stylus-based contact profilometry [70].

The mean value of several measurements carried out for each sample over a constant length is usually used to express the surface roughness of said sample (R_a). Other measures such as R_z and R_t or R_{max} have also been reported in literature as a means to quantify surface roughness of AM parts. R_z is a more sensitive parameter regarding heights and valleys and is the average of the results of measuring the distance between the five highest peaks and the five deepest valley of a number of single distances within one section of measurements. R_t or R_{max} describes the vertical distance between the highest peak and the deepest valley within the section of measurement. These parameters are often used to quantify surface roughness as an effective defect size in fatigue life modeling.

The popular stylus or tactile profilometry method and conventional two-dimensional surface parameters might have shortcomings when capturing the 3D nature of AM surfaces. To thoroughly inspect the surface morphology, two other groups of methods have been mentioned in the literature. These include Confocal Microscopy (CM), Focus Variation Microscopy (FVM) and Atomic Force Microscopy (AFM), generally grouped as Areal topography measurements, and conventional 2D imaging methods such as Optical microscopy and Scanning Electron Microscopy (SEM) [70]. FVM takes a 2D optical image with a limited depth of view and combines it with a vertical scanning process along with an algorithm to combine the multiple images to generate a 3D image of the surface [71]. CM also has the ability create “through-focus” images with “infinite” depth of field by obtaining a series/stack of optical sections, taken at different focal planes [72].

The motivation for the adaptation of these methods is that a reasonable analysis of aperiodic surface structures with only one single profile line is not possible [70]. Some studies conclude that an optical 3D topography measurement by means of a confocal microscope offers a higher statistical significance compared to tactile profilometry [73].

Volumetric or 3D methods have been also recently proposed, claiming that the complete sub-surface details would not be fully captured by these former methods. One example of these sub-surface features is shown in Fig. 9, i.e. a notch-like sub-surface defect not detectable by traditional surface roughness analysis but very detrimental to fatigue performance [45]. High-resolution X-ray computed tomography or Synchrotron Radiation Micro-Tomography (SRμT) have been used for surface characterization in AM and for elaborately obtaining sub-surface details such as sharp notch-like defects which are detrimental for fatigue performance [74] and revealing these kinds of defects. However, a tradeoff between resolution and sample volume that can be scanned in a reasonable amount of time always exists for these 3D methods [75].

3.3. Effects of processing condition and the resulting energy density

Defects such as LOF defects and spherical pores pose a significant challenge for AM parts and as such a significant research effort has been focused on process optimization to reduce the size and population of these defects present in AM parts. Ideally, the energy supplied to the melt pool during the AM process should be enough to generate melt pool overlap depths greater than the layer thickness. Too much or little energy can be associated with over melting or insufficient melting [20,26,31,32,37,48,76,77], as well as a highly dynamic melt pool

Geometry	Down-skin (μm)		Up-skin (μm)	
	R_a	Standard Deviation	R_a	Standard Deviation
D4	22.8	4.1	15.6	2.3
D6	24.2	3.8	17.4	2.8

(b)

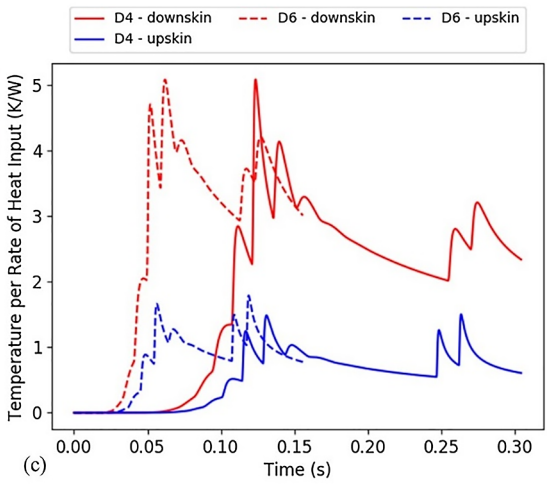

(c)

Fig. 8. (a) Up-skin and down-skin surfaces in relation to the build direction of the as-built LB-PBF Ti-6Al-4V coupons in [60]. (b) The surface roughness measurements of two different geometries, D4 refers to coupons with a gage diameter of 4.00 mm and D6 of 6.06 mm from [45]. (c) Model predictions of the temperature evolution at down-skin and up-skin locations that are 300 μm below the scan layer for the two geometries from [45].

Fig. 9. A notch-like surface defect in a LB-PBF Ti-6Al-4V specimen with cross sectional optical microscopy from Ref. [45].

leading to unstable mass transfer [78,79], all of which can lead to the formation of pores.

When the energy input is insufficient, previous layers are poorly melted, the bonding between consecutively deposited layers is compromised, and LOF defects form between layers. Such defects are typically well-aligned with the deposited layers and are flat, crack-like entities with sharp edges and irregular shape (such as the ones shown in the left image of Fig. 10a [80]). For AM technologies using powder as the feedstock, un-melted particles can often be found in such defects [23]. The sharp edges of these defects lead to stress concentrations, which can reduce the fatigue strength of a Ti-6Al-4V part depending on loading direction [22]. On the other hand, if the input energy is excessive, the melt pool can develop excessive convection currents and stronger vapor recoil forces, resulting in instability and an increase in ejected spatter [78,79]. The unstable melt pool can lead to the formation of voids and/or gas bubbles in the melt pool, which can survive through the solidification process and stay within the solidified Ti-6Al-4V parts (shown in the right image of Fig. 10a). This process is also otherwise referred to as keyholing. The shape of the porosity in this case is generally spherical due to the dominance of surface tension in the liquid metal. The pores may or may not contain gas, depending on whether a shielding gas is used (gas entrapment) and the type of feedstock (the gas containing pores in the powder due to gas atomization process), and may be difficult to remove depending on the solubility of the contained gas [81].

The energy input is typically quantified as a power density (E), which is the amount of energy that is absorbed per unit volume of material per unit time. For the powder bed fusion process, it depends on the power of the heat source (P), energy absorption coefficient (g), deposited thickness (t), hatch spacing (h), and scan speed (V), as seen in the following relationship [37,48,77,82]:

$$E = \frac{gP}{Vht}, \tag{1}$$

For powder fed and wire fed processes, the layer thickness and hatch spacing are coupled with the stock feed rate (volumetric, f) and are not independently controlled; therefore, the power density is expressed as [11]:

$$E = \frac{gP}{Vf}, \tag{2}$$

By adjusting AM process parameters, power density can be tuned as to achieve Ti-6Al-4V parts with optimal relative density. Numerous studies performed on both laser powder bed fusion and electron beam melting systems have reported optimal sets of processing parameters that lead to maximum relative part density. These studies also report that processing parameters corresponding to energy densities that are too high or too low can lead to an increase in porosity [26,31,32,37,48,76,77]. For the data from these studies to be comparable and meaningful, the power density has been normalized based on the optimum value (i.e. E/E_{opt}) and plotted versus the part density relative to their wrought counterparts (ρ/ρ_{wrt}) as its function in Fig. 10b.

Fig. 10b confirms that there exists a window for power density in which an optimum part density as high as 99.99% can be achieved (Region II, corresponding to the center image in Fig. 10a). It should be noted, however, that powder quality plays a role in AM part porosity as well which optimized process parameters may not be able to overcome [83]. On both sides of this window, i.e. in Regions I and III, the relative part density starts to decrease. It may be seen that scatter exists in Regions I and III, even within the same data set. This is mainly due to the energy absorption rate (α) being a function of several parameters,

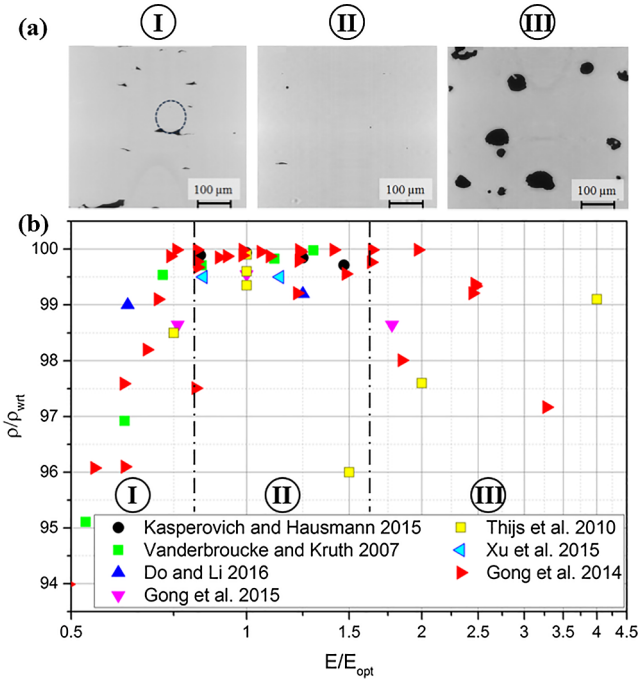

Fig. 10. Variation in relative part density as a function of power density. Part (a) shows typical porosity morphologies [20] that correspond to different power density levels, Part (b) presents data points corresponding to different AM processes, including laser powder bed fusion [26,31,32,37,48,76,77] and EBM [26,37].

such as P, V, f, t, h, etc., and that the true power density is difficult to obtain.

It is important to note that energy density is a first order approach and over simplifies a complex interaction between the material (previously solidified as well as powder) and the energy source. While the approach has been found to be useful as a starting point [81], it begins to break down when considering more complex interactions such as geometry. For example, fine features or overhangs may require lower energy densities than those implemented for internal hatching of larger areas to limit overheating and unstable melt pools.

It has recently been reported that a part, while having a very good relative density, may contain large amounts of LOF defects that are very flat and do not occupy significant volume [22 80]. These LOF defects can be much more detrimental to the mechanical properties of the material as they are often slit or crack shaped with high stress intensities at the edges. This suggests that if porosity is inevitable, a slight shift in power density towards the higher end (Region III) might be beneficial. In this case, although the relative part density decreases, the flat, LOF defects can be replaced by spherical pores, which corresponds to much lower stress concentrations.

3.4. Defect characterization and quality control

Characterization and control of AM defects and their effect on durability of AM parts is a key area of concern that should be dealt with for qualification and certification of safety critical AM parts [84]. Due to the nature of AM defect formation and the inability to fully eliminate them, the susceptibility of AM materials to premature failure as a result of these defects needs to be carefully assessed. To support such an assessment an appropriate characterization of such defects is necessary. Such information can be later used for probabilistic damage tolerant assessments of AM parts based on the exceedance curve for a given class of material defects. Moreover, variability in AM machines process parameters and/or beam source/material interactions can cause inconsistencies in the defects [85], microstructure, and consequently variability in the mechanical performance. Therefore, reliable stochastic techniques should be established to use the data gathered from the characterization process and to account for the prospective variability between various segments of a large component or between various parts manufactured under the same conditions.

The characteristics of defects such as size, morphology, location, and distribution have shown key roles in the fatigue performance of AM fabricated parts. Therefore, reliable methods should be implemented to investigate these parameters. Some common non-destructive methods of particular interest for defect characterization are the Archimedes method, gas pycnometry, and X-ray Computed Tomography (CT) [86]. Archimedes method and gas pycnometry, while widely used, are not capable of capturing some of the most critical information regarding severity of the defect such as size, location, and distribution. X-ray CT, on the other hand, can resolve defects in 3D space giving quantitive information on their volume, location, and distribution, in addition to tracking the effects of post-processing on the defects [87].

X-ray CT, however, is costly, has some limitations in terms of size and density of the part, and based on the resolution of the procedure it might not be able to fully capture microscopic defects or defects due to LOF containing un-melted powder particles. There is a constraint on the resolution of CT scanning based on the size and number of detectors, the size of the X-ray focal spot, and the size of the object of interest which affects the source-object-detector distances. At a given X-ray luminance, there is always a tradeoff between the resolution, field of view, and the noise-to-signal ratio. To stay above the detection limits and not perceiving noise as defects usually a threshold of 8 voxels per volume for the smallest defect is used in analysis software, therefore, typical commercial machines lack sufficient resolution for pores with diameters less than 10 μm [87,88]. Nevertheless, voxel sizes as low as 0.8 μm has also been reported in a study by Slotwinski et al. [89]. These levels of accuracy increase the cost of the CT scan process, requiring high energy and prolonged scan times if the field of view and signal to noise level is held constant.

Alongside the 3D defect analysis methods such as CT scanning, a simple destructive method, such as microscopic cross-section (serial sectioning) analysis performed on AM parts or witness specimens built

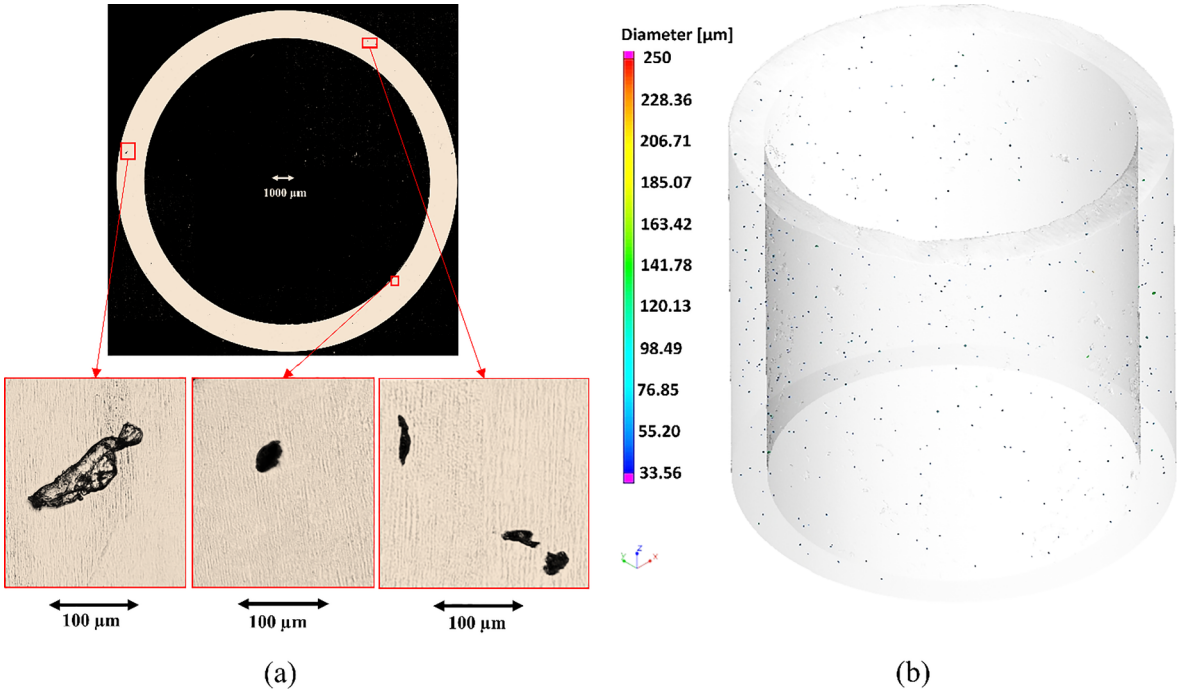

Fig. 11. (a) 2D defect characterization, image gathered by high magnification Digital Microscopy on polished section of a tubular LB-PBF Ti-6Al-4V annealed machined specimen, (b) 3D defect characterization by high resolution (~14 μm voxel size) micro-CT of a 10 mm long portion of gage section of a tubular LB-PBF Ti-6Al-4V annealed machined specimen.

together with the AM part using optical microscopy or SEM, may be beneficial in terms of achieving high resolutions and accuracy in measuring size, shape and location of the microscopic defects [80]. However, these methods provide only the size/shape of defects on the cutting plane. To provide more insight into the data each of these methods, Fig. 11 shows results from both 2D and 3D analysis of the defects of a tubular LB-PBF Ti-6Al-4V annealed and machined specimen. The 3D analysis provides a wide variety of defect characteristics such as location, shape, diameter, and volume. Based on the resolution and the size of defects existing in the specimen, 2D analysis provides complimentary insight into the morphology of a defect with irregular shape on aspects such as whether it is a LOF defect, contains un-melted particles, or if it consists of a series of connected round gas porosities.

Fig. 12 presents the relationship between three important defect characteristics gathered from the defect analysis, namely circularity, aspect ratio and diameter. Defect diameter indicates the diameter of the circumscribed sphere of the defect in 3D analysis and the longest distance between any two points along the selection boundary in 2D analysis. Defect circularity is a measure of irregularity of the defect shape in 2D analysis and is equal to $4\pi(\text{area}/\text{perimeter}^2)$. Defect sphericity is a measure of irregularity of the defect shape in 3D analysis and is equal to the ratio between the surface area of a sphere with the same volume as the defect and the surface area of the defect. Defect aspect ratio is the ratio of the smallest projected size to the largest projected size of the bounding box surrounding the defect in 3D analysis and aspect ratio of the minor/major axes of the fitted ellipse in 2D analysis.

Fig. 12 shows defects larger than about 35 μm in diameter from 3D analysis and defects larger than about 10 μm from 2D analysis. Most of the defects smaller than 35 μm observed in 2D analysis have a circularity equal to or larger than 0.7, which generally corresponds to spherical gas entrapped porosity. These defects are not observed in 3D analysis because, to stay away from false detections imposed by the resolution limits (14 μm), each detected defects were limited to contain at least 8 voxels in volume. The largest defects detected in both 2D and 3D analysis seem to have both low circularity/sphericity and aspect ratio, which results in higher stress concentrations, making them more detrimental to fatigue performance. A high number of moderately large defects were observed in 3D analysis, but not observed on the polished surface for 2D analysis. The higher the number of cross sections investigated in 2D defect analysis, the better the perception gathered on the spatial distribution of the defects would be. However, the randomness of the dispersion of defects along with size and irregularity of the defects shape could affect how accurate the details gathered from 2D analysis can be [85].

The distribution of critical defects is an important factor that requires significant attention for both quantifying and qualifying the fatigue properties of AM parts. The predictability of the precise defect content of AM parts may be low as explained in previous sections due to the high number of parameters involved in the powder composition, manufacturing process and post-processing [90]. It is generally believed that a larger defect is more likely to cause failure compared to a smaller one and the fatigue strength of a component is governed by the largest defects [91], although the sensitivity of the material to defect characteristics such as size is a function of microstructure, defect location, and environmental and mechanical loading conditions. The proximity of the defects to the surface could affect the local stress at the defect even under uniaxial loading conditions. The maximum stress intensity factor in uniaxial fatigue loading for an internal defect can be approximated as $K_{max} = 0.5\sigma\sqrt{\pi\sqrt{area}}$ and for surface defects is approximated as $K_{max} = 0.65\sigma\sqrt{\pi\sqrt{area}}$, where σ is the nominal applied stress and *area* is the defect area normal to the applied stress [92]. This means that, considering two defects of similar size and shape with one at the surface and the other internal, the surface defect would be considered more detrimental to the fatigue resistance than the internal defect.

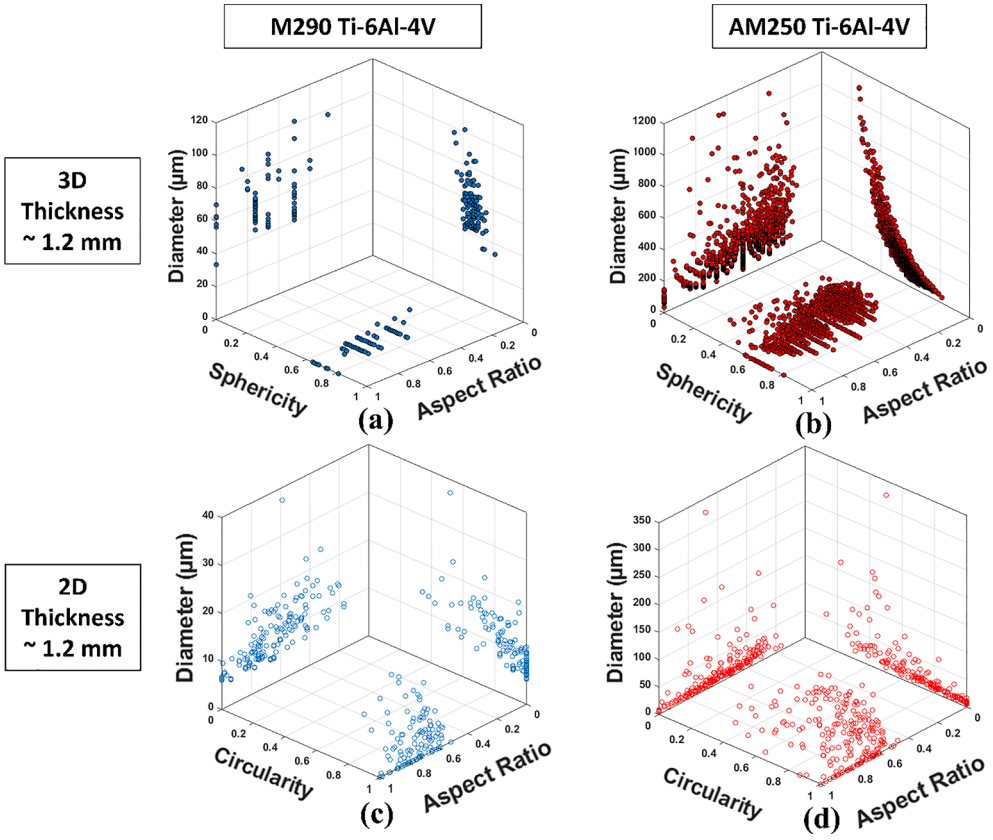

Fig. 12. (a), (b) 3D defect analysis results on sphericity, aspect ratio, and defect diameter from reconstructed model after high resolution (~14 μm voxel size) Micro-CT of a 10 mm long portion of gage section of a tubular LB-PBF Ti-6Al-4V annealed machined specimen manufactured by M290 and AM250 machines, respectively. (c), (d) results from 2D defect analysis on circularity, aspect ratio, and defect diameter from high magnification Digital Microscopy image from a polished section of a tubular LB-PBF Ti-6Al-4V annealed machined specimen manufactured by M290 and AM250 machines, respectively [85].

3.5. Statistical analysis of defects and extreme value statistics

To avoid defect characterization of every AM part, approximation of the maximum prospective defect size is beneficial to predict fatigue performance in the presence of defects. Various representations of the probability distribution functions have been used throughout literature to evaluate the distribution of defects in AM parts [93,94]. It is known that the possibility of finding the largest expected defect induced in a specimen could differ from that in a component. Therefore, the concept of Extreme Value Statistics (EVS) was implemented to estimate the largest expected defect in a larger volume considering the population of defects in a limited number of samples. This is accomplished by focusing on the upper tail of the defect distribution. Murakami [95] had developed an EVS method to predict the maximum inclusion size in a large volume of steel based on Gumbel distribution and Shi et al. [96] later applied a variation of EVS, based on the Generalized Pareto Distribution (GPD), to carry out this prediction.

Romano et al. [97] applied EVS for analyzing X-ray CT scan measurements to qualify ALSi10Mg AM parts. They observed the variability of the defect size distributions using probability plots. Considering the cubic root of the volume or the square root of the projected area as the geometry factor, they observed that the data points over a certain size tend to align, implying that defect sizes exceeding a threshold can be fitted by an exponential distribution, as was previously confirmed for inclusions in steels.

Gumbel distribution function is presented as:

$$F_G(x) = \exp\left(-\left(-\exp\left(\frac{x-\lambda}{\delta}\right)\right)\right) \quad (3)$$

In order to calculate the location parameter λ and scale parameter δ, an estimator of the Cumulative Distribution Function (CDF) of defect sizes is linearized according to the Gumbel distribution. The ability of the Gumbel distribution to fit the data can be interpreted as the quality of the fit in this linearized space. If the resulting plot is almost linear, the data follows a Gumbel distribution where the slope and the intercept are equal to $1/\delta$ and $-\lambda/\alpha$, respectively. The maximum expected defect size in a prospective volume is then computed with $T = V_p/V_{ref}$ as the returning period of maximum defect size in Vp:

$$\sqrt{area_{max}}(V_p) = \lambda - \delta\ln\left(-\ln\left(1-\frac{1}{T}\right)\right) \quad (4)$$

The GPD function is described as:

$$F_{GP}(x) = 1 - \left(1 + \gamma\frac{x-u}{\sigma}\right)^{-1/\gamma} \quad (5)$$

where γ and σ are shape and scale parameters, respectively, and u is the threshold value. This method is used by generating a mean excess (ME) value plot for the defect sizes. The Pareto distribution is characterized by a mean excess function that is roughly linear after the threshold u. The slope of this linear part of the mean excess plot is $\gamma/(1-\gamma)$ with intercept at $\sigma/(1-\gamma)$. The calculated maximum expected defect size tends to an upper limit, as opposed to the first method which uses Gumbel distribution:

$$\sqrt{area}_{max} = u - \frac{\sigma}{\gamma} \quad (6)$$

Based on literature and our analysis, the effect of choosing various threshold values on the final predicted value is not significant. To consider this slight effect, results from various thresholds would be calculated and averaged. The GPD function has been shown to be suitable for EVS using data gathered from 3D defect characterization.

EVS results for two micro-CT scanned Ti-6Al-4V specimens, one annealed and one HIP'ed, using Gumbel distribution are shown in Fig. 13 [97]. Block maxima sampling was used such that a 10 mm length of each specimen's gage section was divided into 8 sub-volumes and the largest defect in each sub-volume was selected. The maximum expected defect diameter for the total specimen gage volume for each case is marked on the plot. The expected maximum defect calculated for HIP'ed condition is about half of that for the annealed condition. The expected maximum defect sizes calculated from EVS methods for various conditions will be later implemented for fatigue life prediction in Part II.

3.6. Effects of powder feedstock and scan strategies on defects

Powder feedstock has also been found to affect the porosity and the resulting mechanical properties of AM materials. Currently, significant efforts in quantifying the effect of powder feedstock on mechanical properties of AM parts is underway. Several studies have attempted to link powder properties such as particle size distribution, shape, roughness, microstructure, and the resulting flowability, compressibility, and aeration to mechanical properties [98–100]. Liu et al. [101] showed that a narrower particle size distribution increased the flowability of the powder and resulted in parts with increased hardness and tensile strength. The increase in flowability was attributed to the reduction of agglomerates, which increase the friction between flowing particles, since particles of similar size tend to flow independently. Nandwana et al. [102] also reported variations in particle size distribution affected the porosity of EBM Ti-6Al-4V with coarser powder sizes leading to more porosity and lower fatigue lives. Interestingly, a

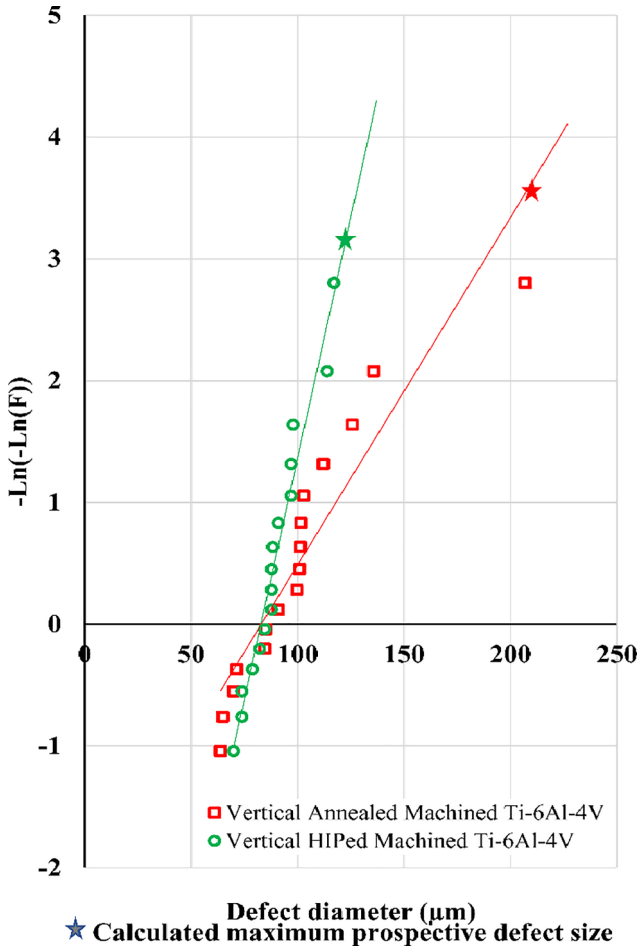

Fig. 13. Gumbel plot for distribution of the largest defect sizes gathered with block maxima sampling from gage section of annealed and HIP'ed tubular LB-PBF Ti-6Al-4V machined surface specimens from two micro-CT scanned specimens for each condition, each divided into eight sub-volumes in the build direction. The calculated maximum prospective defect diameter using Gumbel plots in the volume of one specimen is represented by a star for each case.

wider particle size distribution was shown to increase the final density of the parts due to finer particles filling the vacancies between larger particles. These results suggest that the ideal particle size distribution is wide enough to give good powder bed density yet narrow enough to not degrade the flowability of the powder and that initial powder quality could be highly influential on part performance.

Complementary to powder quality studies is the effect of powder recycling or reconditioning on the mechanical properties of additive manufactured parts. For Ti-6Al-4V AM materials the increase of interstitial elements such as hydrogen, nitrogen, and oxygen are of relative concern. The introduction of these interstitial elements in titanium alloys have been shown to significantly reduce ductility while increasing strength, as well as its susceptibility to stress-corrosion cracking. Studies have reported that increased powder recycling can increase these interstitial elements [103] while others have reported no significant change in interstitial element composition [104,105]. Roach et al. [105] showed that after greater than 20 iterations with periodic reconditioning there was only a small (< 0.01 wt%) increase in interstitial elements. The resulting test coupons fabricated from new and used powder showed similar microstructure and slow strain rate tensile behavior in chloride environments.

The particle size distribution has been reported to significantly change after the recycling of Ti-6Al-4V powder. Seyada et al. [106] reported that after 12 recycling cycles the number of finer particles ($< 20\,\mu m$) decreased while the number of larger particles increased. Parts fabricated after 12 iterations showed less porosity and was reported to be a result of increased flowability due to reduction of agglomerates. The surface roughness, however, was reported to increase for the recycled powder. O'Leary et al. reported similar observations on the particle size distribution along with very little increase in interstitial elements, however, for the fabricated parts they reported an increase in oxygen above the allowable 0.2 wt% specified in ASTM F2924 [107].

The improved defect distribution for recycled powder was also shown by Carrion et al. [108] which led to improved high cycle fatigue behavior of AM Ti-6Al-4V test coupons. In this study a narrower particle size distribution was reported after 15 recycling iterations which improved the flowability of the powder agreeing with the previous research [106]. Fractography of failed high cycle fatigue (HCF) specimens revealed smaller defects responsible for crack initiation for the specimens fabricated from the recycled powder and compared to specimens fabricated from new powder. These interesting results indicate that the powder quality, especially after several recycling steps, is of significant concern for AM Ti-6Al-4V parts. There are currently a limited number of studies that tackle the effect of powder recycling and its effect on the mechanical properties of AM parts. In addition, the multitude of various process parameters and procedures compounds with the complexity of relating powder characteristics to mechanical properties and ultimately part performance.

Scanning strategies have also been investigated regarding their effect on achieving part densities that surpass what is achievable solely through energy density optimization. Tammas-Williams et al. [109] suggested that for an EBM method, the interior hatching of a selectively melted area was responsible for the generation of most defects. It was suggested that pores are pushed along the solidification front of the melt pool, after which they are dumped once the beam changes direction. This results in aggregation of pores at the edges of the hatch lines. At the contour of the melted area, however, the formation of pores was not observed and concluded to be a result of a contour remelting strategy allowing gas-entrapped pores an opportunity to escape. This work suggested that employing different scan strategies or re-melting layers could be beneficial in improving the overall density of fabricated parts, even though this may increase build time. In fact, Gustmann et al. [110] showed that re-melting entire layers of a Cu-Al-Ni-Mn shape memory alloy led to increased relative density and improved ductility.

In addition to improving the defect distribution throughout an AM part, scan strategies are also used to manage the introduction to residual stresses that are inherent to the rapid cooling of LB-PBF. AM systems mostly deal with residual stresses by rotating the laser direction after each layer is melted. The changing direction of the laser results in the successive layer to change the directionality of the residual stress in relation to the previous layer due to the scanning direction. In addition to this rotation of the laser direction, each part slice is often broken into smaller segments or strips reducing the overall length of the laser scanning vector allowing each layer to compensate for the anisotropic effect of the previous layer [111]. A more in-depth discussion on the effects of residual stresses and how to deal with them is given in Section 5.1.

4. In-situ monitoring and real time control of AM process

Understanding that microstructure and defects inherent to the AM process can significantly affect the mechanical behavior of AM parts, there has been a recent surge of interest in real time (in-situ) process monitoring. The multitude of process variables associated with AM technology can make even qualitative assessment of process quality difficult. There are several key signatures from the laser, powder, and part interaction leading to a melt pool that serves as a source of electromagnetic signals that can be readily measured to provide pertinent information on size, shape, stability, and temperature of the meltpool. Most importantly, since the shape and stability of the melt pool can be critical to final part quality, any variability in predetermined process parameters that affect the geometry and temperature of the melt pool can result in insufficient melting leading to poor part quality.

Researchers have implemented pyrometers, photodiodes, high-speed cameras, or a combination of these instruments to investigate several melt pool or AM related properties [112,113]. The systems are either set up in a Lagrangian [114–120] frame of reference that tracks the melt pool directly or an Eulerian [121–124] frame of reference that maintains a constant field of view of within the build area. Lagrangian systems have shown success in monitoring melt pool characteristics but has the drawback of an inability to capture the thermal history of particular areas of interest. The ability to monitor the melt pool directly allows for these types of systems to be implemented in microstructural control applications as suggested by Gockel et al. [8]. Craeghs et al. [122] showed early success in transforming a photodiode detector signal into meaningful data that related to the melt pool area, length, and width. These researchers were able to reduce laser power in real time to prevent overheating. Combining this ability with the process maps generated by Gockel et al. (Fig. 7) [8] real time feedback control of the microstructure may be obtainable. Additionally, feedforward information such as geometry and location of a part can be used to make real time parameter adjustments to improve part characteristics/properties i.e. surface quality at overhangs or functionally graded microstructure at critical locations.

Eulerian reference monitoring systems are popular for their ability to capture thermal history as well as powder distribution quality during fabrication. Researchers have shown the ability to capture porosity by monitoring areas of insufficient melting through an IR camera [124,125]. By monitoring the radiation of the build areas, Schwerdtfeger et al. [125] was able to correlate regions of high radiation with part flaws. These large area monitoring systems, however, are often coupled with a reduction in spatial resolution. This reduced resolution may make detecting critical flaws in fatigue applications difficult due to their small size yet high impact on fatigue resistance.

Data management is possibly the biggest hurdle for practical in situ monitoring of the AM process. Spears and Gold [113] calculated, as reference, the amount of data that would be generated for a Lagrangian melt pool sensor at a data rate of 50 kHz for a 3-day build time to be over 200 gigabytes. Factor on top of this an industrialized manufacturing process and one can see how the amount of generated data can quickly become unmanageable.

The current state of in-situ monitoring is mostly quality assurance to

verify that predefined process variables are maintained or to identify areas with high probabilities of defects after the data has been sufficiently analyzed. One of the most significant challenges that in-situ monitoring offers to overcome is extensive ex-situ qualification of AM parts. Currently, time intensive qualification processes rely on destructive and non-destructive evaluation techniques to ensure part quality. By incorporating monitoring systems that can provide accurate defect information, the extensive time and monetary cost associated with conventional process/part qualification may be significantly reduced. Finally, one of the most rewarding promises of in-situ monitoring is to achieve the ability to implement real time adjustments to maintain desired conditions or repair low quality areas through closed-loop control. Craeghs et al. [122,126] showed early success at implementing such feedback control systems. However, the use of in-situ closed loop control has not been readily proven in the literature. Development of such real time quality control tools through in-situ monitoring has been suggested as a high priority for research by the National Institute of Standards and Technology (NIST) [127] as well as the Department of Defense [128].

5. Post-processing treatments

Despite the progress made in AM process optimization, additional post-processing is often necessary for fatigue critical parts. The effect of post-process thermal treatments on the microstructure of wrought Ti-6Al-4V has been extensively investigated resulting in several well established heat treatment and annealing procedures capable of generating a variety of microstructures and mechanical properties. These procedures, however, were developed using heavily worked and mill annealed material in which the initial microstructure is broken down to an equiaxed α microstructure with β along the grain boundaries. After shaping the alloy through conventional rolling or forging processes a final heat treatment is performed to obtain a desired microstructure dependent on the final application.

5.1. Stress relieving

As mentioned previously, residual stresses are often formed in AM parts due to the large thermal gradients that arise between the previous layers and the melted layer. The cooler solidified layers previously deposited laterally restrict the thermal expansion of the layers above, often within the plastic regime due to the high melting temperatures. Once these moderately compressed layers cool and begin shrinking themselves, they tend to bend upwards but again are restricted by the previous layers resulting in a tensile residual stress component at the surface acting parallel to the build direction. The residual stress adds up with each successive layer until the stress is so high that the previous layers or support structure attaching the part to the substrate fails causing the part to bend upwards and likely lead to build failure. Even in the absence of this build failure, successful builds that manage to resist the buildup of residual stresses during the fabrication process can release these stresses upon removal of the substrate and have excessive dimensional inaccuracies.

While much effort has been given to scan strategies as a means to reduce residual stress during fabrication, stress relieving parts before removal from the substrate is still often a critical post-processing step. Even with the reduction of process induced residual stresses, stress relief is often necessary for parts that require high dimensional accuracy as well as the removal of the detrimental effects of the residual stresses for fatigue and fracture critical parts. Stress relieving temperatures are often much lower than the critical/recrystallization temperature so that the microstructure is mostly unaltered. Baufeld et al. [49] showed that stress relieving treatments at 600 °C for 4 h did not significantly affect either the microstructure or mechanical properties of wire AM Ti-6Al-4V.

While reduction of residual stresses is strongly recommended, particularly in fatigue critical applications, it is imperative to understand the effects of process-induced residual stresses for applications that require AM part deployment in the as-built condition, such as those in remote locations. Edwards and Ramulu [23] showed that the process-induced residual stressed in LB-PBF Ti-6Al-4V are tensile at the surface of as-built parts. For larger parts, the residual stress dropped off to more normal levels, below 100 MPa, at 50 μm below the surface while taller/narrower parts result in higher residual stresses greater than 200 MPa that penetrate up to 250 μm deep. The presence of these residual stresses ultimately resulted in lower fatigue resistance highlighting the importance of fully characterizing the residual stress and its effects for parts that do not undergo post-process stress relief.

5.2. Heat treatment

The heat treatment procedures can be divided into two categories in which the maximum soak temperature is below the β -transus temperature (sub-transus) or above β-transus (super-transus). Sub-transus heat treatments are performed in the α + β field to obtain globular primary α grains in a matrix of secondary α plates. These sub-transus heat treatments and the resulting microstructure give rise to a combination of high strength and ductility. On the other hand, super-transus heat treatments are performed in the β field and result in a fully lamellar or Widmanstätten (basketweave) microstructure which has lower ductility compared to the globular α in transformed β microstructure. The Widmanstatten microstructure, however, has higher fracture toughness as a result of the lamellar grains acting as crack deflectors.

As discussed in Section 2, additive manufactured Ti-6Al-4V parts produced by LB-PBF have very fine microstructures, either ultrafine Widmanstatten or martensite, shown in Fig. 1, as a result of the higher cooling rates. Most importantly, the martensitic microstructure is not ideal as the ductility is severely limited by the fine HCP crystall structure and the propensity towards intergranular failure along prior β grain boundaries. Heat treatments are thus necessary for LB-PBF Ti-6Al-4V parts to improve part ductility that meet standard specifications such as ASTM F1472 and F2924 [107,129]. The unique combination of columnar prior β grain structure and the fine acicular martensitic grains contained within, however, results in insufficient mechanical properties for LB-PBF Ti-6Al-4V when using traditional heat treatment procedures [39–42].

The reduced effectiveness of traditional heat treatments on LB-PBF Ti-6Al-4V to obtain similar mechanical properties, compared to wrought Ti-6Al-4V, is attributed to the unique columnar prior β and α′ microstructure in which the partial dissolution of the α′ phase into α + β acts to restrict any significant grain growth at temperatures below β -transus [41,42,80]. Vrancken et al. [42] showed that successive sub-transus heat treatments at 780 °C, 850 °C, and 950 °C at a soak time of two hours and furnace cooled resulted in equilibrium α + β phase with increasing β phase associated with increasing soak temperature. The width of the α plates were shown to be mainly influenced by the maximum soak temperature, however, for temperatures approaching β-transus the hold time becomes influential as well [80]. Heat treatments that approach the β-transus temperature show increased sensitivity to cooling rate as well as lower cooling rates resulting in coarser α plates, however, the maximum soak temperature is still the most influential aspect of the final α plate width [41,42]. While these sub-transus heat treatments effectively eliminated the martensitic microstructure, the columnar prior β microstructure is preserved.

Vilaro et al. [41] showed that solution annealing treatments above β transus can result in a shearing mechanism from the $\beta \rightarrow \alpha'$ transformation effectively eliminating the columnar prior β microstructure. Vrancken et al. [42] also showed that holding temperatures above β transus results in grain growth along the width of the prior β grains leading to a semi-equiaxed microstructure. For heat treatments that surpass the β -transus temperature, the cooling rate becomes the most

influential aspect on the final microstructure [41,42]. Furnace cooling after super-transus heat treatments have been shown to result in the Widmanstatten microstructure for LB-PBF Ti-6Al-4V [40–42]. While this basketweave microstructure results in inferior ductility compared to the fully lamellar α + β microstructure obtained from the sub-transus heat treatments, it is expected to provide better performance in fracture critical applications.

To obtain the best combination of strength and ductility for Ti-6Al-4V alloys, a bimodal microstructure is often desired. For wrought Ti-6Al-4V alloys this is achieved by thermomechanical processing, however, for AM alloys net shape or near net shape parts are preferred to reduce processing steps. Ter Haar and Becker [40] showed that a bimodal microstructure could be achieved for AM Ti-6Al-4V by taking advantage of the fragmentation that occurs in the α phase during high solid solution temperature region annealing procedure. This allows for globularization of the α phase that is retained after quenching and a subsequent low solid solution temperature region annealing procedure. The low solid solution temperature region anneal allows for the decomposition of the α′ phase to a lamellar α + β microstructure. This bimodal microstructure was shown to greatly improve the ductility of LB-PBF Ti-6Al-4V [40].

HIP treatments may also be a necessary post-process treatment for Ti-6Al-4V parts fabricated by additive manufacturing techniques due to the inherent porosity associated with AM. It has been established that AM Ti-6Al-4V parts subjected to HIP treatment and a subsequent surface machining have high cycle fatigue performance on par with traditional wrought materials [3,130–133]. The improvements in fatigue resistance for HIP'ed AM Ti-6Al-4V components can be attributed to a combination of improved local microstructure surrounding defects and a reduction in defect size [80,131,134]. Li et al. [131] showed via quantitative analysis of electron backscatter diffraction (EBSD) images the existence of a more refined microstructure near defects in the HIP'ed material (Fig. 14). This is consistent with observations in HIP compaction of Ti-6Al-4V powder [134–137] and the microstructure evolution that occurs during the typical wrought Ti-6Al-4V processing route [138–141]. The study [131] suggested that the improved HCF performance by HIP treatment is a combination of decreasing defect sizes below a threshold and changing the microstructure that surrounds defects.

Standard HIP processes for wrought materials may not be applicable for additive materials as they typically involve a post HIP heat treatment. For LB-PBF, the introduction of inert gases such as Ar restricts full healing of the pores as Ar does not easily diffuse through the microstructure [81]. During HT of LB-PBF parts the reduction of the pore size compresses the Ar resulting in a residual pressure in the pore and a tensile residual stress along the pore boundary. Successive heat treatments after HIP may re-open these pores due to the residual pressure introduced by the compression of Ar filled pores reversing some of the benefits of the HIP treatment [109]. This again highlights the need for AM specific post-processing HT schedules that take into account the inter-relationships between process-structure-property (PSP) of additive manufactured parts. Regardless, if heat treatment or HIP is required, stress relieving is often necessary to prevent parts from distorting after removal from the plate.

6. Summary and conclusions

By reviewing and extracting data from the open literature, this work has attempted to summarize what is known regarding process - structure relationships of additive manufactured Ti-6Al-4V. These relationships were elucidated through understanding the relationships between AM processing parameters, post-process treatments, and the resulting phase structures, grain structures and porosity characteristics.

As reviewed, an optimum processing window exists in AM for yielding maximum part density, however, lack-of-fusion defects, which are flat and often unmeasurable via standard density measurement methods, may still exist at relatively high part densities. A compromise in density may be needed in favor of potentially less detrimental

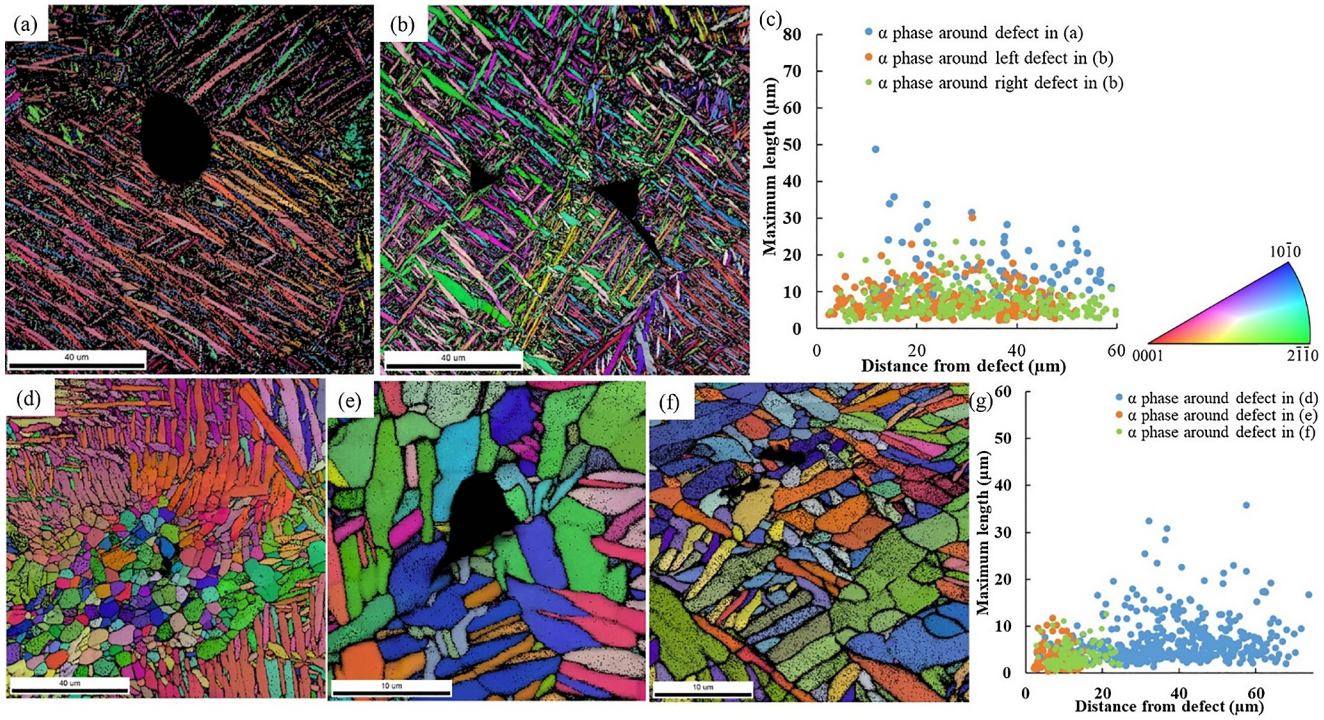

Fig. 14. (a & b) EBSD α phase orientation maps around three defects in LB-PBF Ti-6Al-4V prior to HIP treatment. (c) Scatter plot showing the maximum length of α grains in the scanned plane as a function of the distance to the center of the defect in (a & b). (d, e & f) EBSD α phase orientation maps near defects in HIP treated LB-PBF Ti-6Al-4V. (g) Scatter plot showing the maximum length of α grains in the scanned plane as a function of the distance to the center of the defect in (d, e & f) (where in (f) only the top right pore was analyzed). EBSD maps were collected by cross-sectioning the specimen perpendicular to the build direction (and specimen loading axis). Crystal orientations in the inverse pole fig. (IPF) map are normal to the cross section. Images are adapted from [131].

defects, achievable through the use of higher power density during the manufacturing process. Additionally, additive manufactured-induced lack-of-fusion defects, as well as the aggregates of spherical pores, may produce a weak plane perpendicular to the build direction. Therefore, depending on the presence of lack-of-fusion voids, strong anisotropy in fatigue behavior of AM Ti-6Al-4V may exist. Even within an optimized process window, variations in process and powder conditions can significantly affect the size and distribution of the defects and the resulting mechanical performance of additively manufactured materials.

Depending on cooling rates inherent to a particular AM process, a broad range of phase structures can be produced, including coarse $\alpha + \beta$ lamellar (heat treatment induced), basket weave (Widmanstätten) and the martensitic structures. Coarser microstructures may lead to reduced tensile strength and HCF resistance due to the wider lamellar and larger α-colonies/prior-β grains, respectively. Monitoring or controlling the melt pool size may lead to the ability to custom tailor microstructure for a desired application. As improvements in in-situ monitoring and ultimately closed loop control occur, the ability fabricate a functionally graded microstructure could be realized delivering a long awaited promise of the AM process.

Post-process treatments are often necessary to reduce residual stress and/or improve the microstructure and the defect distribution in AM Ti-6Al-4V. Conventional post-process thermal processing for wrought Ti-6Al-4V, such as annealing/heat treatment and hot isostatic pressing, do not typically give similar results for additive manufactured Ti-6Al-4V parts as a result of their unique as fabricated microstructure. While successful thermal treatments have been shown to result in a variety of microstructures that are comparable to traditional wrought microstructures, leading to comparable mechanical properties, these procedures contrast significantly to the conventional Ti-6Al-4V heat treatments.

Given its physical origins, the fatigue behavior of AM Ti-6Al-4V is highly sensitive to many variables associated with the additive manufacturing process. The unique microstructure as well as the defects associated with additive manufactured Ti-6Al-4V parts makes fatigue life prediction inherently more difficult compared to wrought Ti-6Al-4V. To this point, a thorough review on the characterization of AM Ti-6Al-4V fatigue behavior, which is carried out in Part II of this series, is necessary to detail not only the complex nature of fatigue behavior in regard to AM but also the varying degrees of fatigue performance observed for different AM processes, procedures, and systems. Understanding the PSP relationships and specifically how they relate to the fatigue behavior of Ti-6Al-4V parts is critical for the advancement of additive manufacturing technology.

Declaration of Competing Interest

The authors declare that they have no known competing financial interests or personal relationships that could have appeared to influence the work reported in this paper.

Acknowledgement

This material, in part, is based upon work supported by the U.S. Department of Energy, Office of Science, Office of Basic Energy Sciences, under Award Number DE-SC0019378 and National Science Foundation, under Award Number 1657195. DHW acknowledges financial support from ONR contract #N000141712035. Partial funding of U.S. Naval Air Systems Command (NAVAIR) is also greatly appreciated. VGSTUDIO MAX 3.1 software license was provided by Volume Graphics.

Disclaimer

References

[1] Shamsaei N, Yadollahi A, Bian L, Thompson SM. An overview of Direct Laser Deposition for additive manufacturing. Part II: Mechanical behavior, process parameter optimization and control. Addit Manuf 2015;8:12–35.
[2] Thompson SM, Bian L, Shamsaei N, Yadollahi A. An overview of Direct Laser Deposition for additive manufacturing. Part I: Transport phenomena, modeling and diagnostics. Addit Manuf 2015;8:36–62.
[3] Frazier WE. Metal additive manufacturing: a review. J Mater Eng Perform 2014;23(6):1917–28.
[4] Gu DD, Meiners W, Wissenbach K, Poprawe R. Laser additive manufacturing of metallic components: materials, processes and mechanisms. Int Mater Rev 2012;57(3):133–64.
[5] E. Herderick, Additive manufacturing of metals: A review, Materials Science and Technology (MS); 2011. p.1413.
[6] ASTM International. ASTM ISO/ASTM52900-15 Standard Terminology for Additive Manufacturing – General Principles – Terminology. West Conshohocken, PA: ASTM International; 2015.
[7] Brandt M. Laser additive manufacturing: materials, design,technologies, and applications. Woodhead Publishing; 2016.
[8] Gockel J, Beuth J. Understanding Ti-6Al-4V microstructure control in additive manufacturing via process maps. Solid Freeform Fabrication Proceedings, Austin, TX; Aug (2013): p. 12–14.
[9] Gu R, Ngan AHW. Effects of pre-straining and coating on plastic deformation of aluminum micropillars. Acta Mater 2012;60(17):6102–11.
[10] Lütjering G, Williams JC. Titanium. Springer; 2003.
[11] Wu X, Liang J, Mei J, Mitchell C, Goodwin PS, Voice W. Microstructures of laser-deposited Ti–6Al–4V. Mater Des 2004;25(2):137–44.
[12] Al-Bermani SS, Blackmore ML, Zhang W, Todd I. The origin of microstructural diversity, texture, and mechanical properties in electron beam melted Ti-6Al-4V. Metall Mater Trans A 2010;41(13):3422–34.
[13] Gockel J, Beuth J, Taminger K. Integrated control of solidification microstructure and melt pool dimensions in electron beam wire feed additive manufacturing of Ti-6Al-4V. Addit Manuf 2014;1–4:119–26.
[14] Tao G, Xia Z. Mean stress/strain effect on fatigue behavior of an epoxy resin. Int J Fatigue 2007;29(12):2180–90.
[15] Hall JA. Fatigue crack initiation in alpha-beta titanium alloys. Int J Fatigue 1997;19(93):23–37.
[16] Antonysamy AA, Meyer J, Prangnell PB. Effect of build geometry on the β-grain structure and texture in additive manufacture of Ti6Al4V by selective electron beam melting. Mater Charact 2013;84:153–68.
[17] Bagheri A, Mahtabi MJ, Shamsaei N. Fatigue behavior and cyclic deformation of additive manufactured NiTi. J Mater Process Technol 2018;252:440–53.
[18] Blackwell PL. The mechanical and microstructural characteristics of laser-deposited IN718. J Mater Process Technol 2005;170(1–2):240–6.
[19] Gong H, Rafi K, Karthik NV, Starr T, Stucker B. Defect morphology in Ti-6Al-4V parts fabricated by selective laser melting and electron beam melting. Solid Freeform Fabrication Proceedings, Austin, TX; Aug 2018.
[20] Kasperovich G, Haubrich J, Gussone J, Requena G. Correlation between porosity and processing parameters in TiAl6V4 produced by selective laser melting. Mater Des 2016;105:160–70.
[21] Mahtabi MJ, Shamsaei N, Mitchell MR. Fatigue of Nitinol: the state-of-the-art and ongoing challenges. J Mech Behav Biomed Mater 2015;50:228–54.
[22] Yadollahi A, Shamsaei N, Thompson SM, Elwany A, Bian L. Effects of building orientation and heat treatment on fatigue behavior of selective laser melted 17–4 PH stainless steel. Int J Fatigue 2017;94:218–35.
[23] Edwards P, Ramulu M. Fatigue performance evaluation of selective laser melted Ti–6Al–4V. Mater Sci Eng, A 2014;598:327–37.
[24] Facchini L, Magalini E, Robotti P, Molinari A. Microstructure and mechanical properties of Ti-6Al-4V produced by electron beam melting of pre-alloyed powders. Rapid Prototyping J 2009;15(3):171–8.
[25] Facchini L, Magalini E, Robotti P, Molinari A, Höges S, Wissenbach K. Ductility of a Ti-6Al-4V alloy produced by selective laser melting of prealloyed powders. Rapid Prototyping J 2010;16(6):450–9.
[26] Gong H, Rafi K, Gu H, Ram GJ, Starr T, Stucker B. Influence of defects on mechanical properties of Ti–6Al–4 V components produced by selective laser melting and electron beam melting. Mater Des 2015;86:545–54.
[27] Leuders S, Thöne M, Riemer A, Niendorf T, Tröster T, Richard HA, et al. On the

mechanical behaviour of titanium alloy TiAl6V4 manufactured by selective laser melting: Fatigue resistance and crack growth performance. Int J Fatigue 2013;48:300–7.
[28] Murr LE, Esquivel EV, Quinones SA, Gaytan SM, Lopez MI, Martinez EY, et al. Microstructures and mechanical properties of electron beam-rapid manufactured Ti–6Al–4V biomedical prototypes compared to wrought Ti–6Al–4V. Mater Charact 2009;60(2):96–105.
[29] Murr LE, Quinones SA, Gaytan SM, Lopez MI, Rodela A, Martinez EY, et al. Microstructure and mechanical behavior of Ti–6Al–4V produced by rapid-layer manufacturing, for biomedical applications. J Mech Behav Biomed Mater 2009;2(1):20–32.
[30] Qiu C, Ravi GA, Dance C, Ranson A, Dilworth S, Attallah MM. Fabrication of large Ti–6Al–4V structures by direct laser deposition. J Alloy Compd 2015;629:351–61.
[31] Vandenbroucke B, Kruth J-P. Selective laser melting of biocompatible metals for rapid manufacturing of medical parts. Rapid Prototyping J 2007;13(4):196–203.
[32] Xu W, Brandt M, Sun S, Elambasseril J, Liu Q, Latham K, et al. Additive manufacturing of strong and ductile Ti–6Al–4V by selective laser melting via in situ martensite decomposition. Acta Mater 2015;85:74–84.
[33] Zhai Y, Galarraga H, Lados DA. Microstructure evolution, tensile properties, and fatigue damage mechanisms in Ti-6Al-4V alloys fabricated by two additive manufacturing techniques. Procedia Eng 2015;114:658–66.
[34] Sterling AJ, Torries B, Shamsaei N, Thompson SM, Seely DW. Fatigue behavior and failure mechanisms of direct laser deposited Ti–6Al–4V. Mater Sci Eng, A 2016;655:100–12.
[35] Wycisk E, Siddique S, Herzog D, Walther F, Emmelmann C. Fatigue performance of laser additive manufactured Ti–6Al–4V in very high cycle fatigue regime up to 109 cycles. Front Mater 2015;2.
[36] Li P, Warner D, Fatemi A, Phan N. Critical assessment of the fatigue performance of additively manufactured Ti–6Al–4V and perspective for future research. Int J Fatigue 2016;85:130–43.
[37] Gong H, Rafi K, Gu H, Starr T, Stucker B. Analysis of defect generation in Ti–6Al–4V parts made using powder bed fusion additive manufacturing processes. Addit Manuf 2014;1–4:87–98.
[38] Leung CLA, Marussi S, Atwood RC, Towrie M, Withers PJ, Lee PD. In situ X-ray imaging of defect and molten pool dynamics in laser additive manufacturing. Nat Commun 2018;9(1):1355.
[39] Brandl E, Greitemeier D. Microstructure of additive layer manufactured Ti–6Al–4V after exceptional post heat treatments. Mater Lett 2012;81:84–7.
[40] Ter Haar GM, Becker TH. Selective laser melting produced Ti-6Al-4V: post-process heat treatments to achieve superior tensile properties. Materials 2018;11(1):146.
[41] Vilaro T, Colin C, Bartout JD. As-fabricated and heat-treated microstructures of the Ti-6Al-4V alloy processed by selective laser melting. Metall Mater Trans A 2011;42(10):3190–9.
[42] Vrancken B, Thijs L, Kruth J-P, Van Humbeeck J. Heat treatment of Ti6Al4V produced by Selective Laser Melting: Microstructure and mechanical properties. J Alloy Compd 2012;541:177–85.
[43] Molaei R, Fatemi A, Phan N. Significance of hot isostatic pressing (HIP) on multiaxial deformation and fatigue behaviors of additive manufactured Ti-6Al-4V including build orientation and surface roughness effects. Int J Fatigue 2018;117:352–70.
[44] Torries B, Shao S, Shamsaei N, Thompson SM. Effect of Inter-Layer Time Interval on the Mechanical Behavior of Direct Laser Deposited Ti-6Al-4V. Solid Freeform Fabrication Proc 2016:1272–82.
[45] Li P, Warner DH, Pegues JW, Roach MD, Shamsaei N, Phan N. Towards predicting differences in fatigue performance of laser powder bed fused Ti-6Al-4V coupons from the same build. Int J Fatigue 2019;126:284–96.
[46] Fatemi A, Molaei R, Simsiriwong J, Sanaei N, Pegues J, Torries B, et al. Fatigue behaviour of additive manufactured materials: An overview of some recent experimental studies on Ti-6Al-4V considering various processing and loading direction effects. Fatigue Fract Eng Mater Struct 2019;42(5):991–1009.
[47] Liu S, Shin YC. Additive manufacturing of Ti6Al4V alloy: A review. Mater Des 2019;164:107552.
[48] Do DK, Li P. The effect of laser energy input on the microstructure, physical and mechanical properties of Ti-6Al-4V alloys by selective laser melting. Virtual Phys Prototyping 2016;11(1):41–7.
[49] Baufeld B, Brandl E, van der Biest O. Wire based additive layer manufacturing: Comparison of microstructure and mechanical properties of Ti–6Al–4V components fabricated by laser-beam deposition and shaped metal deposition. J Mater Process Technol 2011;211(6):1146–58.
[50] Ahmed T, Rack HJ. Phase transformations during cooling in α + β titanium alloys. Mater Sci Eng, A 1998;243(1):206–11.
[51] Sieniawski J, Ziaja W, Motyka KKAM. Microstructure and mechanical properties of high strength two-phase titanium alloys. Titanium Alloys - Advances in Properties Control; 2013.
[52] Grujicic M, Dang P. Atomic-scale analysis of martensitic transformation in titanium alloyed with vanadium Part I: verification of the embedded-atom method model. Mater Sci Eng, A 1996;205(1):139–52.
[53] Rafi HK, Karthik NV, Gong H, Starr TL, Stucker BE. Microstructures and mechanical properties of Ti6Al4V parts fabricated by selective laser melting and electron beam melting. J Mater Eng Perform 2013;22(12):3872–83.
[54] Barrett CR, Nix WD, Tetelman AS. The principles of engineering materials. Prentice Hall; 1973.
[55] Callister WD, Rethwisch DG. Materials science and engineering: an introduction. New York: Wiley; 1991.
[56] Wu SQ, Lu YJ, Gan YL, Huang TT, Zhao CQ, Lin JJ, et al. Microstructural evolution and microhardness of a selective-laser-melted Ti–6Al–4V alloy after post heat treatments. J Alloy Compd 2016;672:643–52.
[57] Kobryn PA, Semiatin SL. The laser additive manufacture of Ti-6Al-4V. JOM 2001;53(9):40–2.
[58] Kobryn PA, Semiatin SL. Microstructure and texture evolution during solidification processing of Ti–6Al–4V. J Mater Process Technol 2003;135(2):330–9.
[59] Hunt JD. Steady state columnar and equiaxed growth of dendrites and eutectic. Mater Sci Eng 1984;65(1):75–83.
[60] Pegues J, Roach M, Williamson RS, Shamsaei N. Surface roughness effects on the fatigue strength of additively manufactured Ti-6Al-4V. Int J Fatigue 2018;116:543–52.
[61] Pegues JW, Shamsaei N, Roach MD, Williamson RS. Fatigue life estimation of additive manufactured parts in the as-built surface condition,. Mater Des Process Commun 2019:e36.
[62] Moylan S, Slotwinski J, Cooke A, Jurrens K, Donmez MA. Proposal for a standardized test artifact for additive manufacturing machines and processes. In: Proceedings of the 2012 annual international solid freeform fabrication symposium. Austin, TX; 2012.
[63] Strano G, Hao L, Everson RM, Evans KE. Surface roughness analysis, modelling and prediction in selective laser melting. J Mater Process Technol 2013;213(4):589–97.
[64] El-Sayed M, Ghazy M, Yehia Y, Essa K. Optimization of SLM Process Parameters for Ti6Al4V Medical Implants.
[65] Mumtaz K, Hopkinson N. Top surface and side roughness of Inconel 625 parts processed using selective laser melting. Rapid Prototyping J 2009;15(2):96–103.
[66] Gong H, Rafi K, Starr T, Stucker B. The effects of processing parameters on defect regularity in Ti-6Al-4V parts fabricated by selective laser melting and electron beam melting. In: 24th Annual International Solid Freeform Fabrication Symposium—An Additive Manufacturing Conference, Austin, TX; Aug. 2013.
[67] Shrestha R, Simsiriwong J, Shamsaei N, Thompson SM, Bian L. Effect of build orientation on the fatigue behavior of stainless steel 316L manufactured via a laser-powder bed fusion process. In: 27th Annual Solid Frefform Fabrication Symposium Proceedings; 2016.
[68] Triantaphyllou A, Giusca CL, Macaulay GD, Roerig F, Hoebel M, Leach RK, et al. Surface texture measurement for additive manufacturing. Surf Topogr Metrol Prop 2015;3(2):024002.
[69] Charles A, Elkaseer A, Müller T, Thijs L, Torge M, Hagenmeyer V, et al. A study of the factors influencing generated surface roughness of down-facing surfaces in selective laser melting. In; Proceedings of the World Congress on Micro and Nano Manufacturing (WCMNM), Portorož, Slovenia; 2018.
[70] Townsend A, Senin N, Blunt L, Leach R, Taylor J. Surface texture metrology for metal additive manufacturing: a review. Precis Eng 2016;46:34–47.
[71] Newton L, Senin N, Gomez C, Danzl R, Helmli F, Blunt L, et al. Areal topography measurement of metal additive surfaces using focus variation microscopy. Addit Manuf 2019;25:365–89.
[72] Safdar A, He H, Wei L-Y, Snis A, Chavez de Paz LE. Effect of process parameters settings and thickness on surface roughness of EBM produced Ti-6Al-4V. Rapid Prototyping J 2012;18(5):401–8.
[73] Grimm T, Wiora G, Witt G. Characterization of typical surface effects in additive manufacturing with confocal microscopy. Surf Topogr Metrol Prop 2015;3(1):014001.
[74] Kantzos C, Cunningham R, Tari V, Rollett A. Characterization of metal additive manufacturing surfaces using synchrotron X-ray CT and micromechanical modeling. Comput Mech 2018;61(5):575–80.
[75] Thompson A, Maskery I, Leach RK. X-ray computed tomography for additive manufacturing: a review. Meas Sci Technol 2016;27(7):072001.
[76] Kasperovich G, Hausmann J. Improvement of fatigue resistance and ductility of TiAl6V4 processed by selective laser melting. J Mater Process Technol 2015;220:202–14.
[77] Thijs L, Verhaeghe F, Craeghs T, Humbeeck JV, Kruth J-P. A study of the microstructural evolution during selective laser melting of Ti–6Al–4V. Acta Mater 2010;58(9):3303–12.
[78] King WE, Anderson AT, Ferencz RM, Hodge NE, Kamath C, Khairallah SA, et al. Laser powder bed fusion additive manufacturing of metals; physics, computational, and materials challenges. Appl Phys Rev 2015;2(4):041304.
[79] Ly S, Rubenchik AM, Khairallah SA, Guss G, Matthews MJ. Metal vapor micro-jet controls material redistribution in laser powder bed fusion additive manufacturing. Sci Rep 2017;7(1):4085.
[80] Zhang B, Meng WJ, Shao S, Phan N, Shamsaei N. Effect of heat treatments on pore morphology and microstructure of laser additive manufactured parts. Mater Des Process Commun 2019;1(1):e29.
[81] Shao S, Mahtabi MJ, Shamsaei N, Thompson SM. Solubility of argon in laser additive manufactured α-titanium under hot isostatic pressing condition. Comput Mater Sci 2017;131:209–19.
[82] Prashanth KG, Scudino S, Maity T, Das J, Eckert J. Is the energy density a reliable parameter for materials synthesis by selective laser melting? Mater Res Lett 2017;5(6):386–90.
[83] Carrion PE, Shamsaei N. Strain-based fatigue data for Ti–6Al–4V ELI under fully-reversed and mean strain loads. Data in Brief 2016;7:12–5.
[84] Seifi M, Gorelik M, Waller J, Hrabe N, Shamsaei N, Daniewicz S, et al. Progress towards metal additive manufacturing standardization to support qualification and certification. JOM 2017;69(3):439–55.
[85] Sanaei N, Fatemi A, Phan N. Defect characteristics and analysis of their variability in metal L-PBF additive manufacturing. Mater Des 2019;108091.
[86] Wits WW, Carmignato S, Zanini F, Vaneker TH. Porosity testing methods for the quality assessment of selective laser melted parts. CIRP Ann 2016;65(1):201–4.
[87] Shui X, Yamanaka K, Mori M, Nagata Y, Kurita K, Chiba A. Effects of post-

processing on cyclic fatigue response of a titanium alloy additively manufactured by electron beam melting. Mater Sci Eng, A 2017;680:239–48.
[88] Seifi M, Salem A, Satko D, Shaffer J, Lewandowski JJ. Defect distribution and microstructure heterogeneity effects on fracture resistance and fatigue behavior of EBM Ti–6Al–4V. Int J Fatigue 2017;94:263–87.
[89] Slotwinski JA, Garboczi EJ, Hebenstreit KM. Porosity measurements and analysis for metal additive manufacturing process control. J Res Nat Inst Stand Technol 2014;119:494.
[90] Smith J, Xiong W, Yan W, Lin S, Cheng P, Kafka OL, et al. Linking process, structure, property, and performance for metal-based additive manufacturing: computational approaches with experimental support. Comput Mech 2016;57(4):583–610.
[91] Murakami Y, Beretta S. Small defects and inhomogeneities in fatigue strength: experiments, models and statistical implications. Extremes 1999;2(2):123–47.
[92] Murakami Y. Metal fatigue: effects of small defects and nonmetallic inclusions. Academic Press; 2019.
[93] Günther J, Krewerth D, Lippmann T, Leuders S, Tröster T, Weidner A, et al. Fatigue life of additively manufactured Ti–6Al–4V in the very high cycle fatigue regime. Int J Fatigue 2017;94:236–45.
[94] Tang M. Inclusions, porosity, and fatigue of AlSi10Mg parts produced by selective laser melting. Carnegie Mellon University; 2017.
[95] Murakami Y. Inclusion rating by statistics of extreme values and its application to fatigue strength prediction and quality control of materials. J Res-Natl Instit Standards Technol 1994;99. 345–345.
[96] Shi G, Atkinson H, Sellars C, Anderson C. Application of the generalized Pareto distribution to the estimation of the size of the maximum inclusion in clean steels. Acta Mater 1999;47(5):1455–68.
[97] Romano S, Brandão A, Gumpinger J, Gschweitl M, Beretta S. Qualification of AM parts: Extreme value statistics applied to tomographic measurements. Mater Des 2017;131:32–48.
[98] Benson JM, Snyders E. The need for powder characterisation in the additive manufacturing industry and the establishment of a national facility. S Afr J Ind Eng 2015;26(2):104–14.
[99] Sutton AT, Kriewall CS, Leu MC, Newkirk JW. Powders for additive manufacturing processes: Characterization techniques and effects on part properties. In: Proceedings of the 26th Annual International Solid Freeform Fabrication Symposium–An Additive Manufacturing Conference; 2016.
[100] Sutton AT, Kriewall CS, Leu MC, Newkirk JW. Powder characterisation techniques and effects of powder characteristics on part properties in powder-bed fusion processes. Virtual Phys Prototyping 2017;12(1):3–29.
[101] Liu B, Wildman R, Tuck C, Ashcroft I, Hague R. Investigation the effect of particle size distribution on processing parameters optimisation in selective laser melting process. Additive Manufacturing Research Group, Loughborough University; 2011. p. 227–38.
[102] Nandwana P, Kirka MM, Paquit VC, Yoder S, Dehoff RR. Correlations between powder feedstock quality, in situ porosity detection, and fatigue behavior of Ti-6Al-4V fabricated by powder bed electron beam melting: a step towards qualification. JOM 2018;70(9):1686–91.
[103] Sun Y, Aindow M, Hebert RJ. The effect of recycling on the oxygen distribution in Ti-6Al-4V powder for additive manufacturing. Mater High Temp 2018;35(1–3):217–24.
[104] O'Leary R, Setchi R, Prickett PW. An investigation into the recycling of Ti-6Al-4V powder used within SLM to improve sustainability; 2015.
[105] Roach MD, Williamson RS, Zardiackas LD. Comparison of the corrosion fatigue characteristics of CP Ti-Grade 4, Ti-6AI-4V ELI, Ti-6AI-7Nb, and Ti-15Mo. ASTM International; 2006.
[106] Seyda V, Kaufmann N, Emmelmann C. Investigation of aging processes of Ti-6Al-4V powder material in laser melting. Phys Procedia 2012;39:425–31.
[107] ASTM International. ASTM F2924–14 Standard Specification for Additive Manufacturing Titanium-6 Aluminum-4 Vanadium with Powder Bed Fusion. West Conshohocken, PA: ASTM International; 2014.
[108] Carrion PE, Sultani-Tehrani A, Phan N, Shamsaei N. Powder recycling effects on the tensile and fatigue behavior of additively manufactured Ti-6Al-4V parts. JOM 2019;71(3):963–73.
[109] Tammas-Williams S, Zhao H, Léonard F, Derguti F, Todd I, Prangnell PB. XCT analysis of the influence of melt strategies on defect population in Ti–6Al–4V components manufactured by Selective Electron Beam Melting. Mater Charact 2015;102:47–61.
[110] Gustmann T, Neves A, Kühn U, Gargarella P, Kiminami C, Bolfarini C, et al. Influence of processing parameters on the fabrication of a Cu-Al-Ni-Mn shape-memory alloy by selective laser melting. Addit Manuf 2016;11:23–31.
[111] Vrancken B, Cain V, Knutsen R, Van Humbeeck J. Residual stress via the contour method in compact tension specimens produced via selective laser melting. Scr Mater 2014;87:29–32.
[112] Everton SK, Hirsch M, Stravroulakis P, Leach RK, Clare AT. Review of in-situ process monitoring and in-situ metrology for metal additive manufacturing. Mater Des 2016;95:431–45.
[113] Spears TG, Gold SA. In-process sensing in selective laser melting (SLM) additive manufacturing. Integr Mater Manuf Innov 2016;5(1):2.
[114] Berumen S, Bechmann F, Lindner S, Kruth J-P, Craeghs T. Quality control of laser- and powder bed-based Additive Manufacturing (AM) technologies. Physics Procedia 2010;5:617–22.
[115] Chivel Y, Smurov I. On-line temperature monitoring in selective laser sintering/melting. Phys Procedia 2010;5:515–21.
[116] Clijsters S, Craeghs T, Buls S, Kempen K, Kruth J-P. In situ quality control of the selective laser melting process using a high-speed, real-time melt pool monitoring system. Int J Adv Manuf Technol 2014;75(5–8):1089–101.
[117] Craeghs T, Clijsters S, Kruth J-P, Bechmann F, Ebert M-C. Detection of process failures in layerwise laser melting with optical process monitoring. Phys Procedia 2012;39:753–9.
[118] Lott P, Schleifenbaum H, Meiners W, Wissenbach K, Hinke C, Bültmann J. Design of an optical system for the in situ process monitoring of selective laser melting (SLM). Phys Procedia 2011;12:683–90.
[119] Pavlov M, Doubenskaia M, Smurov I. Pyrometric analysis of thermal processes in SLM technology. Phys Procedia 2010;5:523–31.
[120] Yadroitsev I, Krakhmalev P, Yadroitsava I. Selective laser melting of Ti6Al4V alloy for biomedical applications: Temperature monitoring and microstructural evolution. J Alloy Compd 2014;583:404–9.
[121] Alldredge J, Slotwinski J, Storck S, Kim S, Goldberg A, Montalbano T. In-situ monitoring and modeling of metal additive manufacturing powder bed fusion. AIP Conference Proceedings. AIP Publishing; 2018, p. 020007.
[122] Craeghs T, Clijsters S, Yasa E, Kruth J-P. Online quality control of selective laser melting. In: Proceedings of the Solid Freeform Fabrication Symposium, Austin, TX; 2011.
[123] Grünberger T, Domröse R. Optical In-Process Monitoring of Direct Metal Laser Sintering (DMLS) A revolutionary technology meets automated quality inspection. Laser Tech J 2014;11(2):40–2.
[124] Krauss H, Eschey C, Zaeh M. Thermography for monitoring the selective laser melting process. In: Proceedings of the Solid Freeform Fabrication Symposium; 2012.
[125] Schwerdtfeger J, Singer RF, Körner C. In situ flaw detection by IR-imaging during electron beam melting. Rapid Prototyping J 2012;18(4):259–63.
[126] Craeghs T, Bechmann F, Berumen S, Kruth J-P. Feedback control of Layerwise Laser Melting using optical sensors. Phys Procedia 2010;5:505–14.
[127] Measurement science roadmap for metal-based additive manufacturing, Workshop Summary Report, National Institute of Standards and Technology, Maryland; 2012, pp. 4–5.
[128] Fielding J, Davis A, Bouffard B, Kinsella M, Delgado T, Wilczynski J, et al. Department of defense additive manufacturing roadmap. Washington, DC: US Department of Defense; 2016.
[129] ASTM International. ASTM F1472–14 Standard Specification for Wrought Titanium-6Aluminum-4Vanadium Alloy for Surgical Implant Applications (UNS R56400). West Conshohocken, PA: ASTM International; 2014.
[130] Froes F, Dutta B. The additive manufacturing (AM) of titanium alloys. Advanced Materials Research, Trans Tech Publ; 2014. p. 19–25.
[131] Li P, Warner D, Pegues J, Roach M, Shamsaei N, Phan N. Investigation of the mechanism by which hot isostatic pressing improves the fatigue performance of powder bed fused Ti-6Al-4V. Int J Fatigue 2018.
[132] Popov V, Katz-Demyanetz A, Garkun A, Muller G, Strokin E, Rosenson H. Effect of hot isostatic pressure treatment on the electron-beam melted Ti-6Al-4V specimens. Procedia Manuf 2018;21:125–32.
[133] Uhlmann E, Kersting R, Klein TB, Cruz MF, Borille AV. Additive manufacturing of titanium alloy for aircraft components. Procedia CIRP 2015;35:55–60.
[134] Xu L, Guo R, Bai C, Lei J, Yang R. Effect of hot isostatic pressing conditions and cooling rate on microstructure and properties of Ti–6Al–4V alloy from atomized powder. J Mater Sci Technol 2014;30(12):1289–95.
[135] Cai C, Song B, Xue P, Wei Q, Wu J-M, Li W, et al. Effect of hot isostatic pressing procedure on performance of Ti6Al4V: surface qualities, microstructure and mechanical properties. J Alloy Compd 2016;686:55–63.
[136] Guo R, Xu L, Wu J, Yang R, Zong BY. Microstructural evolution and mechanical properties of powder metallurgy Ti–6Al–4V alloy based on heat response. Mater Sci Eng, A 2015;639:327–34.
[137] Zhang K, Mei J, Wain N, Wu X. Effect of hot-isostatic-pressing parameters on the microstructure and properties of powder Ti-6Al-4V hot-isostatically-pressed samples. Metall Mater Trans A 2010;41(4):1033–45.
[138] Chen W, Boehlert C, Payzant EA, Howe JY. The effect of processing on the 455 C tensile and fatigue behavior of boron-modified Ti–6Al–4V. Int J Fatigue 2010;32(3):627–38.
[139] Inagaki I, Shirai Y, Cho K, Niinomi M. Effects of Hot Working Conditions on Fatigue Strength of Ti-6Al-4V Alloy. Proceedings of the 13th World Conference on Titanium, Wiley Online Library. 2016. p. 811–5.
[140] Perumal B, Rist MA, Gungor S, Brooks JW, Fitzpatrick ME. The effect of hot deformation parameters on microstructure evolution of the α-phase in Ti-6Al-4V. Metall Mater Trans A 2016;47(8):4128–36.
[141] Semiatin S, Seetharaman V, Weiss I. Flow behavior and globularization kinetics during hot working of Ti–6Al–4V with a colony alpha microstructure. Mater Sci Eng, A 1999;263(2):257–71.
[142] Kirchner A, Klöden B, Luft J, Weißgärber T, Kieback B. Process window for electron beam melting of Ti-6Al-4V. Powder Metall 2015;58(4):246–9.
[143] Brandl E, Leyens C, Palm F. Mechanical Properties of Additive Manufactured Ti-6Al-4V Using Wire and Powder Based Processes. IOP Conf Series: Mater Sci Eng 2011;26(1):012004.
[144] Kirchner A, Klöden B, Weißgärber T, Kieback B, Schoberth A, Bagehorn S, et al. Mechanical properties of Ti-6Al-4V additively manufactured by electron beam melting. In: Proceedings of the European Powder Metallurgy Association 2015 Congress & Exhibition, Reims, France; 2015. p. 4–7.